

# Convection-driven spherical shell dynamos at varying Prandtl numbers

P. J. Käpylä<sup>1,2,3,4</sup>, M. J. Käpylä<sup>3,2</sup>, N. Olsper<sup>2</sup>, J. Warnecke<sup>3</sup>, and A. Brandenburg<sup>4,5,6,7</sup>

<sup>1</sup> Leibniz-Institut für Astrophysik Potsdam, An der Sternwarte 16, D-11482 Potsdam, Germany e-mail: pkapyla@aip.de

<sup>2</sup> ReSoLVE Centre of Excellence, Department of Computer Science, Aalto University, PO Box 15400, FI-00076 Aalto, Finland

<sup>3</sup> Max-Planck-Institut für Sonnensystemforschung, Justus-von-Liebig-Weg 3, D-37077 Göttingen, Germany

<sup>4</sup> NORDITA, KTH Royal Institute of Technology and Stockholm University, Roslagstullsbacken 23, SE-10691 Stockholm, Sweden

<sup>5</sup> Department of Astronomy, AlbaNova University Center, Stockholm University, SE-10691 Stockholm, Sweden

<sup>6</sup> JILA and Department of Astrophysical and Planetary Sciences, Box 440, University of Colorado, Boulder, CO 80303, USA

<sup>7</sup> Laboratory for Atmospheric and Space Physics, 3665 Discovery Drive, Boulder, CO 80303, USA

May 25, 2022, Revision: 1.287

## ABSTRACT

*Context.* Stellar convection zones are characterized by vigorous high-Reynolds number turbulence at low Prandtl numbers.

*Aims.* We study the dynamo and differential rotation regimes at varying levels of viscous, thermal, and magnetic diffusion.

*Methods.* We perform three-dimensional simulations of stratified fully compressible magnetohydrodynamic convection in rotating spherical wedges at various thermal and magnetic Prandtl numbers (from 0.25 to 2 and 5, respectively). Differential rotation and large-scale magnetic fields are produced self-consistently.

*Results.* We find that for high thermal diffusivity, the rotation profiles show a monotonically increasing angular velocity from the bottom of the convection zone to the top and from the poles toward the equator. For sufficiently rapid rotation, a region of negative radial shear develops at mid-latitudes as the thermal diffusivity is decreased, corresponding to an increase of the Prandtl number. This coincides with and results in a change of the dynamo mode from poleward propagating activity belts to equatorward propagating ones. Furthermore, the clearly cyclic solutions disappear at the highest magnetic Reynolds numbers and give way to irregular sign changes or quasi-stationary states. The total (mean & fluctuating) magnetic energy increases as a function of the magnetic Reynolds number in the range studied here (5 – 151), but the energies of the mean magnetic fields level off at high magnetic Reynolds numbers. The differential rotation is strongly affected by the magnetic fields and almost vanishes at the highest magnetic Reynolds numbers. In some of our most turbulent cases, however, we find that two regimes are possible where either differential rotation is strong and mean magnetic fields relatively weak or vice versa.

*Conclusions.* Our simulations indicate a strong non-linear feedback of magnetic fields on differential rotation, leading to qualitative changes in the behaviors of large-scale dynamos at high magnetic Reynolds numbers. Furthermore, we do not find indications of the simulations approaching an asymptotic regime where the results would be independent of diffusion coefficients in the parameter range studied here.

**Key words.** convection – turbulence – dynamos – Magnetohydrodynamics (MHD) – Sun: magnetic fields

## 1. Introduction

Simulations of convection-driven dynamos have recently reached a level of sophistication where they capture effects observed in the Sun such as equatorward migration of activity belts (Schrinner et al. 2011; Käpylä et al. 2012; Augustson et al. 2015; Duarte et al. 2016), and irregular cycle variations such as grand minima and long term modulations (Passos & Charbonneau 2014; Käpylä et al. 2016a). Most of these simulations are individual numerical experiments and it is not clear how they are situated in parameter space in relation to each other. Important parameters in this connection concern the relative strengths of different diffusion coefficients, viscosity ( $\nu$ ), magnetic ( $\eta$ ), and thermal ( $\chi$ ) diffusivities present in the system. Their ratios are characterized by the thermal and magnetic *Prandtl numbers*,  $Pr = \nu/\chi$  and  $Pr_M = \nu/\eta$ , respectively. In the solar convection zone, these Prandtl numbers are  $Pr \ll 1$  and  $Pr_M \ll 1$ , while the fluid and magnetic Reynolds numbers,  $Re = ul/\nu$  and  $Re_M = ul/\eta$ , with  $u$  and  $l$  being the characteristic velocity and length scale, are of the orders of  $10^{12}$  and  $10^9$ , respectively. Such parameter regimes are not accessible to current numeri-

cal simulations which are restricted to  $Pr \approx 1$ ,  $Pr_M \approx 1$ , and Reynolds numbers of the order to  $10^2 \dots 10^3$ . In all simulations by a number of different groups, the dominant contribution to thermal diffusion comes through a subgrid-scale (SGS) coefficient  $\chi_{SGS}$  whose magnitude is much higher than the radiative one. Similar arguments apply also to  $\nu$  and  $\eta$ , but since the functional form of those diffusion operators is unchanged, we omit in those the subscript SGS. Thus, the relevant thermal Prandtl number in simulations is  $Pr_{SGS} = \nu/\chi_{SGS}$ . We emphasize that this applies to simulations of all groups, although the nomenclature may be different (see Table A.1 in Appendix A). This is also true for groups using realistic luminosities, and thus the correct order of magnitude for the radiative diffusivity (e.g. Brun et al. 2004; Hotta et al. 2016).

When the convection simulations of Käpylä et al. (2012) in wedge geometry showed for the first time equatorward migration, it was not yet clear that this was related to their choice of  $Pr_{SGS} = 2.5$  compared with  $Pr_{SGS} \lesssim 1$  used in most earlier simulations that showed either quasi-stationary configurations (Brown et al. 2010) or either weak or poleward migration (e.g.

Ghizaru et al. 2010; Käpylä et al. 2010b; Brown et al. 2011; Gastine et al. 2012). Recently, Warnecke et al. (2014) showed that the change in the dynamo behavior between  $\text{Pr}_{\text{SGS}} > 1$  and  $\text{Pr}_{\text{SGS}} < 1$  regimes is due to a change in the differential rotation profile which, in the  $\text{Pr}_{\text{SGS}} \gtrsim 1$  regime, leads to a region of negative radial shear that facilitates the equatorward migration. Also the magnetic Prandtl number, which is proportional to the magnetic Reynolds number, can strongly affect the results. Increasing  $\text{Re}_M$  by increasing  $\text{Pr}_M$  can allow magnetohydrodynamic (MHD) instabilities such as magnetic buoyancy (Parker 1955) and magnetorotational instabilities (e.g. Parfrey & Menou 2007; Masada 2011) to be excited.

Increasing the magnetic Reynolds number can influence the large-scale dynamo via several other avenues. First, the most easily excited dynamo mode can change. Second, a small-scale dynamo is likely excited after  $\text{Re}_M$  exceeds a threshold value (e.g. Cattaneo 1999), and this may also affect the large-scale dynamo by modifying the velocity field. Third, Boussinesq simulations indicate that differential rotation is strongly quenched as the magnetic Reynolds number increases (Schrunner et al. 2012). This was shown to be associated with a transition from oscillatory multipolar large-scale field configurations to quasi-stationary dipole-dominated dynamos as a function of  $\text{Re}_M$ . One of the main goals of the present paper is therefore to systematically study the effects of varying Prandtl numbers on the differential rotation and dynamo modes excited in the simulations. We note that similar parameter studies have been performed with Boussinesq simulations (e.g. Simitev & Busse 2005; Busse & Simitev 2006). Here we explore the stratified, fully compressible simulations and reach parameter regimes that are significantly more supercritical in terms of both the convection and the dynamo.

Another important aspect is related to the saturation level of the large-scale field in simulations at high  $\text{Re}_M$ . Dynamo theory experienced a crisis in the early 1990s when it was discovered that the energy of the large-scale magnetic field saturates at a level that is inversely proportional to the magnetic Reynolds number (Gruzinov & Diamond 1995; Brandenburg & Dobler 2001). If this were to carry over to the Sun, where the magnetic Reynolds number is of the order of  $10^9$  or greater, only very weak large-scale fields would survive. This phenomenon was related to a *catastrophic quenching* of the  $\alpha$  effect (Cattaneo & Vainshtein 1991; Vainshtein & Cattaneo 1992; Cattaneo & Hughes 1996).

Later, this was understood in terms of magnetic helicity: if the system is closed or fully periodic, i.e. when magnetic field lines do not cross the boundary of the system, no flux of magnetic helicity in or out can occur, and only the *molecular* diffusion can change it (Brandenburg 2001). In astrophysical systems this would mean that magnetic helicity would be nearly conserved. However, astrophysical systems are not closed and magnetic helicity can escape, e.g. via coronal mass ejections in the Sun (e.g. Blackman & Brandenburg 2003; Warnecke et al. 2011, 2012) or via winds from galaxies (Shukurov et al. 2006; Sur et al. 2007; Del Sordo et al. 2013). In mean-field theory these physical effects are parameterized by fluxes, which lead to alleviation of catastrophic quenching in suitable parameter regimes (e.g. Brandenburg et al. 2009).

Direct numerical simulations of large-scale dynamos have demonstrated that open boundaries lead to alleviation of catastrophic quenching in accordance with the interpretation in terms of magnetic helicity conservation (e.g. Brandenburg & Sandin 2004; Käpylä et al. 2010a). Although the large-scale magnetic field amplitude does not decrease proportional to  $\text{Re}_M$  in the

cases when open boundaries are used, there is still a decreasing trend even at the highest currently studied  $\text{Re}_M$  in local simulations of convection-driven dynamos (e.g. Käpylä et al. 2010a). This, however, is compatible with mean-field models which suggest that the magnetic helicity fluxes become effective only at significantly higher  $\text{Re}_M$  (Brandenburg et al. 2009; Del Sordo et al. 2013).

In convective dynamos in spherical coordinates the computational challenge is even greater and systematic parameter scans have not been performed. Some preliminary attempts have been made, but the results remain inconclusive. An illuminating example is the study of Nelson et al. (2013) where the large-scale axisymmetric field decreases by a factor of two when the magnetic Reynolds number is increased by a factor of four, which is still rather steep. In a recent paper, Hotta et al. (2016) show that in even higher- $\text{Re}_M$  simulations the mean magnetic energy recovers and claim that this is a consequence of an efficient small-scale dynamo that suppresses small-scale flows. Another goal of the present paper is therefore to study the saturation level of the large-scale field in convection-driven dynamos in spherical coordinates with and without a simultaneous small-scale dynamo (hereafter SSD).

In the present study, we employ a spherical wedge geometry by imposing either a perfect conductor or a normal field boundary condition at high latitudes. Earlier mean-field simulations of  $\alpha\Omega$  dynamos have suggested that solutions with a perfect conductor boundary condition are similar to those in full spherical shells (Jennings et al. 1990). However, more recent work by Cole et al. (2016) has demonstrated that this conclusion is not generally valid and depends on the nature of the solutions. Their work also suggests that the use of a normal field boundary condition at high latitudes might be a better way of obtaining solutions that are applicable to full spherical shells. Owing to this uncertainty, we investigate here cases with both types of boundary conditions.

## 2. The model

The model is similar to that used in Käpylä et al. (2012) and is described in detail in Käpylä et al. (2013). We study the dynamics of magnetized gas in spherical coordinates where only parts of the latitude and longitude ranges are retained. More specifically, we model a wedge that covers  $r_0 \leq r \leq r_1$  in radius,  $\theta_0 \leq \theta \leq \pi - \theta_0$  in colatitude, and  $0 \leq \phi \leq \phi_0$  in longitude. Here we use  $r_0 = 0.7R_\odot$ ,  $r_1 = R_\odot$ , and where  $R_\odot = 6.96 \cdot 10^8 \text{m}$  is the solar radius,  $\theta_0 = 15^\circ$ , and  $\phi_0 = 90^\circ$ .

We solve the following set of compressible hydromagnetics equations

$$\frac{\partial \mathbf{A}}{\partial t} = \mathbf{U} \times \mathbf{B} - \eta \mu_0 \mathbf{J}, \quad (1)$$

$$\frac{D \ln \rho}{Dt} = -\nabla \cdot \mathbf{U}, \quad (2)$$

$$\frac{D\mathbf{U}}{Dt} = \mathbf{g} - 2\boldsymbol{\Omega}_0 \times \mathbf{U} + \frac{1}{\rho} [\nabla \cdot (2\nu \rho \mathbf{S}) - \nabla p + \mathbf{J} \times \mathbf{B}], \quad (3)$$

$$T \frac{Ds}{Dt} = \frac{1}{\rho} [\eta \mu_0 \mathbf{J}^2 - \nabla \cdot (\mathbf{F}^{\text{rad}} + \mathbf{F}^{\text{SGS}})] + 2\nu \mathbf{S}^2, \quad (4)$$

where  $\mathbf{A}$  is the magnetic vector potential,  $\mathbf{U}$  is the velocity,  $\mathbf{B} = \nabla \times \mathbf{A}$  is the magnetic field,  $\eta$  is the magnetic diffusivity,  $\mu_0$  is the permeability of vacuum,  $\mathbf{J} = \nabla \times \mathbf{B} / \mu_0$  is the current density,  $D/Dt = \partial/\partial t + \mathbf{U} \cdot \nabla$  is the advective time derivative,  $\rho$  is the density,  $\mathbf{g}$  is the acceleration due to gravity and  $\boldsymbol{\Omega}_0 =$

$(\cos \theta, -\sin \theta, 0)\Omega_0$  is the angular velocity vector where  $\Omega_0$  is the rotation rate of the frame of reference,  $\nu$  is the kinematic viscosity,  $p$  is the pressure, and  $s$  is the specific entropy with  $Ds = c_V D \ln p - c_P D \ln \rho$ . The gas is assumed to obey the ideal gas law,  $p = (\gamma - 1)\rho e$ , where  $e = c_V T$  is the specific internal energy and  $\gamma = c_P/c_V$  is the ratio of specific heats at constant pressure and volume, respectively. The rate of strain tensor is given by

$$S_{ij} = \frac{1}{2}(U_{i;j} + U_{j;i}) - \frac{1}{3}\delta_{ij}\nabla \cdot \mathbf{U}, \quad (5)$$

where the semicolons refer to covariant derivatives; see Mitra et al. (2009). The radiative and subgrid-scale (SGS) fluxes are given by

$$\mathbf{F}^{\text{rad}} = -K\nabla T, \quad \mathbf{F}^{\text{SGS}} = -\chi_{\text{SGS}}\rho T\nabla s, \quad (6)$$

where  $K = c_P\rho\chi$  is the heat conductivity, and  $\chi_{\text{SGS}}$  is the (turbulent) subgrid-scale diffusion coefficient for the entropy.

### 2.1. Initial and boundary conditions

We follow the description given in Käpylä et al. (2014) to transform our results into physical units. As our equations are fully compressible we cannot afford to use the solar luminosity which would lead to the sound speed dominating the time step. Thus we increase the luminosity substantially and to compensate we increase the rotation rate to achieve the same rotational influence as in the Sun. Assuming a scaling of the luminosity with the convective energy flux as  $L \propto \rho u^3$ , we find that the convective velocities increase to one third power of the luminosity (e.g. Brandenburg et al. 2005; Karak et al. 2015). The ratio between model and solar luminosities is  $L_0/L_\odot \approx 6.4 \cdot 10^5$  in the current simulations. We correspondingly increase the rotation rate by a factor of  $(L_0/L_\odot)^{\frac{1}{3}} \approx 86$  for the solar case. We reiterate that the main effect of increasing the luminosity is to increase the Mach number and bring the acoustic and dynamical timescales closer to each other, which facilitates the computations with a fully compressible method (cf. Fig. 1 of Käpylä et al. 2013). Another possibility would be to apply the so-called reduced sound speed method where the sound speed is artificially changed so that the Mach number does not become too small at the base of the convection zone (Hotta et al. 2012; Käpylä et al. 2016b).

The higher luminosity also helps to reach a thermal equilibrium within reasonable simulation running time. Furthermore, we assume that the density and the temperature at the base of the convection zone are the same as in the Sun, i.e.  $\rho_{\text{bot}} = 200 \text{ kg m}^{-3}$  and  $T = 2.23 \cdot 10^6 \text{ K}$ .

As the initial condition for the hydrodynamics we use an isentropic atmosphere. The temperature gradient is given by

$$\frac{\partial T}{\partial r} = -\frac{GM_\odot/r^2}{c_V(\gamma - 1)(n_{\text{ad}} - 1)}, \quad (7)$$

where  $G = 6.67 \cdot 10^{-11} \text{ N m}^2 \text{ kg}^{-2}$  is Newton's gravitational constant,  $M_\odot = 1.989 \cdot 10^{30} \text{ kg}$  is the solar mass, and  $n_{\text{ad}} = 1.5$  is the polytropic index for an adiabatic stratification.

The initial state is not in thermal equilibrium but closer to the final convecting state to reduce the time needed to reach a statistically stationary state. The heat conductivity has a profile given by  $K(r) = K_0[n(r) + 1]$ , where  $n(r) = \delta n(r/r_0)^{15} + n_{\text{ad}} - \delta n$ , with  $K_0 = (\mathcal{L}/4\pi)c_V(\gamma - 1)(n_{\text{ad}} + 1)\rho_{\text{bot}}\sqrt{GM_\odot R_\odot}$ , and where  $\mathcal{L}$  is a dimensionless luminosity defined below. We keep  $\delta n = 1.9$  fixed in our simulations resulting a situation where

radiation transports all of the flux into the domain but its contribution diminishes rapidly toward the surface (see, e.g., Fig. 2 of Käpylä et al. 2011a).

The subgrid scale diffusivity  $\chi_{\text{SGS}}$  for the entropy has a piecewise constant profile, such that the value  $\chi_{\text{SGS}} = 6.1 \cdot 10^8 \text{ m}^2 \text{ s}^{-2}$  is fixed above  $r = 0.98R_\odot$  in all runs, and the value  $\chi_{\text{SGS}}^{\text{m}} = \chi_{\text{SGS}}(r = r_m = 0.85R_\odot)$  in the bulk of the convection zone is varied via the corresponding Prandtl number (see below). The value below  $r = 0.75R_\odot$  is set equal to  $0.1\chi_{\text{SGS}}^{\text{m}}$ . The constant values in the different layers connect smoothly over a transition depth of  $d = 0.01R_\odot$ .

The boundary conditions for the flow are assumed to be impenetrable and stress free, i.e.,

$$U_r = 0, \quad \frac{\partial U_\theta}{\partial r} = \frac{U_\theta}{r}, \quad \frac{\partial U_\phi}{\partial r} = \frac{U_\phi}{r} \quad (r = r_0, r_1), \quad (8)$$

$$\frac{\partial U_r}{\partial \theta} = U_\theta = 0, \quad \frac{\partial U_\phi}{\partial \theta} = U_\phi \cot \theta \quad (\theta = \theta_0, \pi - \theta_0). \quad (9)$$

The lower radial boundary is assumed to be perfectly conducting, and on the outer radial boundary the field is purely radial. The latitudinal boundaries are either perfectly conducting (PC) or a normal field (NF) condition is assumed. In terms of the magnetic vector potential these are given by

$$\frac{\partial A_r}{\partial r} = A_\theta = A_\phi = 0 \quad (r = r_0), \quad (10)$$

$$A_r = 0, \quad \frac{\partial A_\theta}{\partial r} = -\frac{A_\theta}{r}, \quad \frac{\partial A_\phi}{\partial r} = -\frac{A_\phi}{r} \quad (r = r_1), \quad (11)$$

$$A_r = \frac{\partial A_\theta}{\partial \theta} = A_\phi = 0 \quad (\theta = \theta_0, \pi - \theta_0) \quad (\text{PC}), \quad (12)$$

$$\frac{\partial A_r}{\partial \theta} = A_\theta = 0, \quad \frac{\partial A_\phi}{\partial \theta} = -\frac{\cot \theta A_\phi}{r} \quad (\theta = \theta_0, \pi - \theta_0) \quad (\text{NF}). \quad (13)$$

For the density and specific entropy we assume vanishing first derivatives on the latitudinal boundaries.

At the lower boundary we specify

$$F_r^{\text{rad}} + F_r^{\text{SGS}} = \frac{L_0}{4\pi r_0^2}, \quad (14)$$

which leads to constant input luminosity into the system. On the outer radial boundary we apply a radiative boundary condition

$$\sigma T^4 = F_r^{\text{rad}} + F_r^{\text{SGS}}, \quad (15)$$

where  $\sigma$  is the Stefan–Boltzmann constant. We use a modified value for  $\sigma$  that takes into account that the luminosity and the temperature at the surface are larger than in the Sun. The value of  $\sigma$  is chosen so that the surface flux,  $\sigma T^4$ , carries the total luminosity through the boundary in the initial non-convecting state.

### 2.2. System parameters and diagnostics quantities

The parameters governing our models are the dimensionless luminosity

$$\mathcal{L} = \frac{L_0}{\rho_0(GM_\odot)^{3/2}R_\odot^{1/2}}, \quad (16)$$

the normalized pressure scale height at the surface,

$$\xi = \frac{(\gamma - 1)c_V T_1}{GM_\odot/R_\odot}, \quad (17)$$

**Table 1.** Summary of the runs.

Run	$\tilde{\Omega}$	Ra[10 <sup>6</sup> ]	Pr	Pr <sub>SGS</sub>	Pr <sub>M</sub>	Ta[10 <sup>8</sup> ]	$\nu$ [10 <sup>8</sup> m <sup>2</sup> s <sup>-1</sup> ]	Re	Pe	Re <sub>M</sub>	Co	$\Delta t$	SSD	BCs	Grid
A1	5	0.8	71.7	0.25	0.25	1.25	1.01	20	5	5	14.0	0.4	–	PC	128 × 256 × 128
A2	5	0.8	71.7	0.25	0.50	1.25	1.01	18	4	9	15.1	0.4	–	PC	128 × 256 × 128
A3	5	0.8	71.7	0.25	1.00	1.25	1.01	17	4	17	15.9	56	–	PC	128 × 256 × 128
A4	5	0.8	71.7	0.25	2.00	1.25	1.01	22	5	45	12.4	37	–	PC	128 × 256 × 128
A5	5	0.8	71.7	0.25	3.33	1.25	1.01	23	5	79	11.7	26	–	NF	256 × 512 × 256
B1	5	2.9	71.7	0.50	0.25	1.25	1.01	25	12	6	11.1	5.5	–	PC	128 × 256 × 128
B2	5	2.9	71.7	0.50	0.50	1.25	1.01	24	12	12	11.3	27	–	PC	128 × 256 × 128
B3	5	2.9	71.7	0.50	1.00	1.25	1.01	27	13	27	10.3	26	–	PC	128 × 256 × 128
B4	5	2.9	71.7	0.50	2.00	1.25	1.01	29	14	58	9.7	50	–	PC	128 × 256 × 128
B5	5	2.9	71.7	0.50	5.00	1.25	1.01	27	13	137	10.3	23	+	NF	256 × 512 × 256
C1	5	10	71.7	1.00	0.25	1.25	1.01	28	28	7	9.9	27	–	PC	128 × 256 × 128
C2	5	10	71.7	1.00	0.50	1.25	1.01	29	29	14	9.6	44	–	PC	128 × 256 × 128
C3	5	10	71.7	1.00	1.00	1.25	1.01	29	29	29	9.4	108	–	PC	128 × 256 × 128
C4	5	10	71.7	1.00	1.43	1.25	1.01	30	30	44	9.1	65	–	PC	128 × 256 × 128
C5	5	10	71.7	1.00	5.00	1.25	1.01	29	29	146	9.6	35	+	NF	256 × 512 × 256
D1	5	36	71.7	2.00	0.25	1.25	1.01	30	60	7	9.3	4.2	–	PC	128 × 256 × 128
D2	5	36	71.7	2.00	0.50	1.25	1.01	29	59	14	9.5	60	–	PC	128 × 256 × 128
D3	5	36	71.7	2.00	1.00	1.25	1.01	29	59	29	9.4	61	–	PC	128 × 256 × 128
D4	5	36	71.7	2.00	2.00	1.25	1.01	29	59	59	9.5	43	+	PC	128 × 256 × 128
D5	5	36	71.7	2.00	3.33	1.25	1.01	29	59	98	9.5	25	+	NF	256 × 512 × 256
E1	3	10	71.7	1.00	0.50	0.45	1.01	33	33	16	5.0	12	–	PC	144 × 288 × 144
E2	3	10	71.7	1.00	1.00	0.45	1.01	34	34	34	4.9	55	–	PC	144 × 288 × 144
E3	3	10	71.7	1.00	2.00	0.45	1.01	32	32	65	5.2	70	+	NF	144 × 288 × 144
E4	3	10	71.7	1.00	4.00	0.45	1.01	33	33	134	5.0	19	+	NF	288 × 576 × 288
F1	1	10	71.7	1.00	0.50	0.05	1.01	40	40	20	1.4	20	–	PC	144 × 288 × 144
F2	1	10	71.7	1.00	1.00	0.05	1.01	39	39	39	1.4	43	–	PC	144 × 288 × 144
F3	1	10	71.7	1.00	2.00	0.05	1.01	38	38	76	1.5	49	+	PC	144 × 288 × 144
F4	1	10	71.7	1.00	4.00	0.05	1.01	37	37	151	1.5	30	+	NF	288 × 576 × 288
G1	5	10	71.7	1.00	1.00	1.25	1.01	29	29	29	9.4	108	–	PC	128 × 256 × 128
G2	5	73	35.9	1.00	1.00	5.00	0.51	66	66	66	8.5	47	+	NF	256 × 512 × 256
G3	5	488	17.9	1.00	1.00	20.01	0.25	134	134	134	8.4	14	+	NF	512 × 1024 × 512

**Notes.** Summary of the runs. Here,  $\tilde{\Omega} = \Omega_0/\Omega_\odot$ , where  $\Omega_\odot = 2.7 \cdot 10^{-6} \text{ s}^{-1}$  is the solar rotation rate,  $\Delta t$  (in years) is the length of the time series considered, and the columns SSD and BCs indicate whether a small-scale dynamo is present and the type of latitudinal magnetic field boundary condition, respectively. The last column indicates the grid resolution. All runs have  $\mathcal{L} = 3 \cdot 10^{-5}$  and  $\xi = 0.02$ . Runs C3 and G1 are the same.

with  $T_1$  being the temperature at the surface in the initial state, the Taylor number

$$\text{Ta} = (2\Omega_0\Delta r^2/\nu)^2, \quad (18)$$

where  $\Delta r = r_1 - r_0 = 0.3 R_\odot$ , as well as the fluid, SGS, and magnetic Prandtl numbers

$$\text{Pr} = \frac{\nu}{\chi_m}, \quad \text{Pr}_{\text{SGS}} = \frac{\nu}{\chi_{\text{SGS}}^m}, \quad \text{Pr}_M = \frac{\nu}{\eta}, \quad (19)$$

where  $\chi_m = K(r_m)/c_P\rho_m$  is the thermal diffusivity and  $\rho_m$  is the density, both evaluated at  $r = r_m$ . We keep  $\text{Pr} = 71.7$  fixed and vary  $\text{Pr}_{\text{SGS}}$  and  $\text{Pr}_M$  in most of our models, with the exception of Set G where  $\text{Pr}_{\text{SGS}}$  and  $\text{Pr}_M$  are set to unity and  $\text{Pr}$  is varied by changing the value of  $\nu$  (see Table 1). The Rayleigh number is defined as

$$\text{Ra} = \frac{GM_\odot(\Delta r)^4}{\nu\chi_{\text{SGS}}^m R_\odot^2} \left( -\frac{1}{c_P} \frac{ds_{\text{hs}}}{dr} \right)_{r_m}, \quad (20)$$

where  $s_{\text{hs}}$  is the entropy in the hydrostatic (hs), non-convecting state obtained from a one-dimensional model where no convection can develop with the prescriptions of  $K$  and  $\chi_{\text{SGS}}$  given above.

The remaining parameters are used only as diagnostics. These include the fluid and magnetic Reynolds numbers, and the Péclet number

$$\text{Re} = \frac{u_{\text{rms}}}{\nu k_f}, \quad \text{Re}_M = \frac{u_{\text{rms}}}{\eta k_f}, \quad \text{Pe} = \frac{u_{\text{rms}}}{\chi_{\text{SGS}}^m k_f}, \quad (21)$$

where  $k_f = 2\pi/\Delta r \approx 21R_\odot^{-1}$  is an estimate of the wavenumber of the largest eddies. Rotational influence on the flow is given by the Coriolis number

$$\text{Co} = \frac{2\Omega_0}{u_{\text{rms}} k_f}, \quad (22)$$

where  $u_{\text{rms}} = \sqrt{(3/2)\langle U_r^2 + U_\theta^2 \rangle_{r\theta\phi t}}$  is the rms velocity and the subscripts indicate averaging over  $r$ ,  $\theta$ ,  $\phi$ , and a time interval during which the run is thermally relaxed. We omit the contribution from the azimuthal velocity in  $u_{\text{rms}}$ , because it is dominated by differential rotation (Käpylä et al. 2011b).

We define mean quantities as averages over the  $\phi$ -coordinate and denote them by overbars. We also often average the data in time over the period of the simulations where thermal energy, differential rotation, and large-scale magnetic fields have reached statistically saturated states.

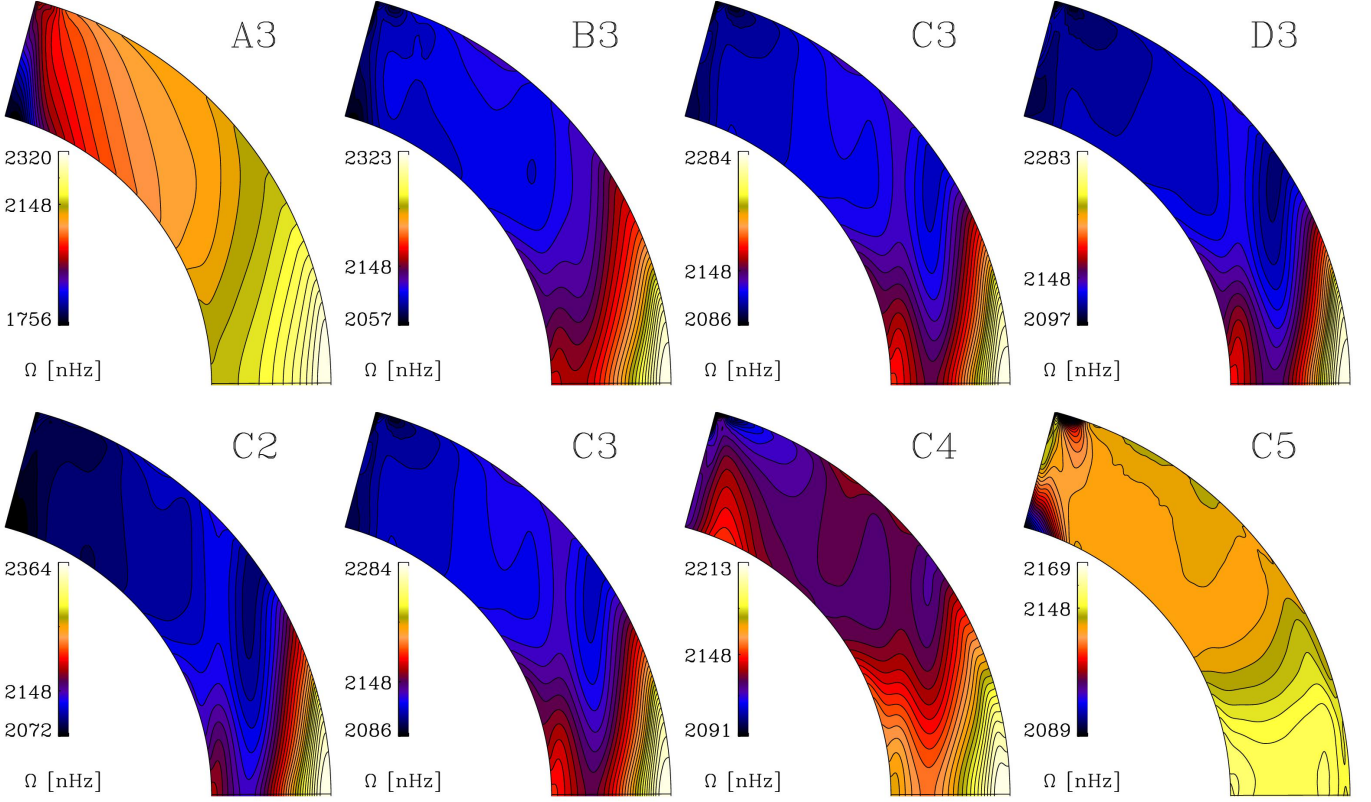


**Fig. 1.** *Top row:* temporally averaged rotation profiles from Runs A3, B3, C3, and D3 with  $\text{Pr}_M = 1$  and  $\text{Pr}_{\text{SGS}}$  varying from 0.25 (left) to 2 (right). *Lower row:* the same as above but for Runs C2, C3, C4, and C5 with  $\text{Pr}_{\text{SGS}} = 1$  and  $\text{Pr}_M$  varying from 0.5 (left) to 5 (right).

The simulations are performed with the PENCIL CODE<sup>1</sup>, which uses a high-order finite difference method for solving the compressible equations of magnetohydrodynamics.

### 3. Data analysis: $D^2$ statistic

To detect possible cycles and to estimate their average lengths we have chosen to use  $D^2$  phase dispersion statistic (Pelt 1983). It has recently been applied to irregularly spaced long-term photometry of solar-like stars (Lindborg et al. 2013; Olsper et al. 2015) as well as to more regularly sampled magnetoconvection simulation data (Karak et al. 2015; Käpylä et al. 2016a). In the previous applications the statistic has been used exclusively on one-dimensional time series (e.g. by fixing a certain latitude and radius in the azimuthally averaged data). In the current study we use a generalized form of the statistic given by

$$D^2(P, \Delta t_{\text{coh}}) = \frac{\sum_{i=1}^{N-1} \sum_{j=i+1}^N g(t_i, t_j, P, \Delta t_{\text{coh}}) \|\mathbf{f}(t_i) - \mathbf{f}(t_j)\|^2}{2\sigma^2 \sum_{i=1}^{N-1} \sum_{j=i+1}^N g(t_i, t_j, P, \Delta t_{\text{coh}})}, \quad (23)$$

where  $\mathbf{f}(t_i)$  is the vector of observed variables at time moment  $t_i$ ,  $\sigma^2 = N^{-2} \sum_{i,j>i} \|\mathbf{f}(t_i) - \mathbf{f}(t_j)\|^2$  is the variance of the full time series,  $g(t_i, t_j, P, \Delta t_{\text{coh}})$  is the selection function, which is significantly greater than zero only when

$$t_j - t_i \approx kP, k = \pm 1, \pm 2, \dots, \quad \text{and} \quad (24)$$

$$|t_j - t_i| \lesssim \Delta t_{\text{coh}} = l_{\text{coh}} P, \quad (25)$$

<sup>1</sup> <http://pencil-code.github.com/>

where  $P$  is the trial period and  $\Delta t_{\text{coh}}$  is the so-called coherence time, which is the measure of the width of the sliding time window wherein the data points are taken into account by the statistic. The number of trial periods fitting into this interval,  $l_{\text{coh}} = \Delta t_{\text{coh}}/P$ , is called a coherence length. With this definition there is no restriction on the dimensionality of the data, but Eq. (23) leaves open the choice of the vector norm. In most cases it is natural to use the Euclidean norm, which we also do in our analysis. We use this statistic to analyze the radial and azimuthal components of the magnetic field at regions near the surface over latitude intervals, where the cycles are the most pronounced (see Sect. 4.2.2).

### 4. Results

We perform six sets of simulations (Sets A–F), each with a constant value of  $\text{Pr}_{\text{SGS}}$  but changing  $\text{Pr}_M$  in the range  $0.25 \leq \text{Pr}_M \leq 5$ ; see Table 1. Furthermore, in an additional Set G we fix  $\text{Pr}_{\text{SGS}} = \text{Pr}_M = 1$  and vary the Reynolds and Péclet numbers. The rotation rate is varied such that Sets A–D and G have  $\Omega_0 = 5\Omega_\odot$ , whereas in Sets E and F we use  $3\Omega_\odot$  and  $\Omega_\odot$ , respectively. Sets E and F are included in order to study the robustness of our findings at slower rotation. In some sets (A, D, E, and F) numerical problems prevented the use of  $\text{Pr}_M = 5$ . In those cases we used a lower value that produces numerically stable solutions. The latitudinal PC boundary conditions lead to numerical problems due to an unidentified instability at high magnetic Reynolds numbers near the latitudinal boundaries. Cases where this occurred have been rerun with the NF conditions. We do not find major qualitative differences in the behavior of the

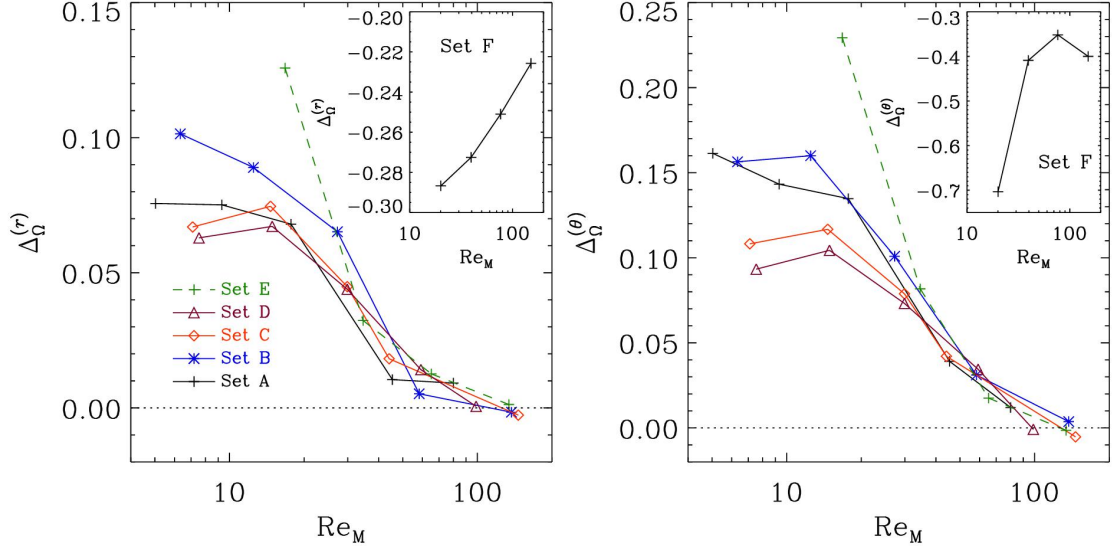


**Fig. 2.** Estimates of radial and latitudinal differential rotation  $\Delta_{\Omega}^{(r)}$  and  $\Delta_{\Omega}^{(\theta)}$ , respectively, according to Eq. (26) for Sets A–F as indicated by the legend.

large-scale field between PC and NF runs with otherwise identical parameters. Furthermore, we omit the  $\text{Pr}_M = 0.25$  runs that do not lead to dynamos in Sets E and F. We note that Run B2 has been presented as Run II in Warnecke et al. (2014), Run D3 as Run A1 in Warnecke et al. (2016a,b), and Run C3 covers the first 120 years of the run presented in Käpylä et al. (2016a). Furthermore, runs similar to Run D3 (but with  $\text{Pr}_M = 2.5$  instead of 2.0) have been presented as Runs B4m and C1 in Käpylä et al. (2012, 2013).

#### 4.1. Large-scale flows and their generators

##### 4.1.1. Differential rotation and meridional circulation

The sign of the radial gradient of  $\Omega$  plays a crucial role in determining the propagation direction of dynamo waves in  $\alpha\Omega$  dynamos: with a positive  $\alpha$  effect in the northern hemisphere, a negative radial gradient of  $\Omega$  is required to obtain solar-like equatorward migration and vice versa (Parker 1955; Yoshimura 1975). It is remarkable that this rule also seems to apply to the fully nonlinear convective dynamo simulations (Warnecke et al. 2014, 2016b). The current simulations can produce equatorward migration only in cases where a region with a negative radial gradient of  $\Omega$  occurs at mid-latitudes (e.g. Käpylä et al. 2012, 2013; Augustson et al. 2015) or if the sign of the kinetic helicity, which is a proxy of the  $\alpha$  effect, is inverted in the bulk of the convection zone (Duarte et al. 2016).

The simulations of Käpylä et al. (2012), Augustson et al. (2015), Käpylä et al. (2016a), and Warnecke et al. (2016a) showing equatorward migration and a region of negative radial shear at mid-latitudes had  $\text{Pr}_{\text{SGS}} \gtrsim 1$ . This is in contrast to earlier simulations with  $\text{Pr}_{\text{SGS}} < 1$ , which did not show equatorward migration (e.g. Brun et al. 2004; Brown et al. 2011; Nelson et al. 2013) and had consistently positive gradients of  $\Omega$ . Given that the dynamo wave propagation is apparently heavily influenced by this, it is important to study the effect that  $\text{Pr}_{\text{SGS}}$  has on the rotation profiles.

We show representative results of the temporally averaged rotation profiles as a function of  $\text{Pr}_{\text{SGS}}$  from Runs A3, B3, C3, and D3 in the top row of Fig. 1. In the lowest SGS Prandtl number case (Run A3), the angular velocity  $\Omega = \Omega_0 + \bar{U}_{\phi}/r \sin \theta$  de-

creases monotonically from the equator toward the poles. Much of the latitudinal variation occurs at high latitudes near the latitudinal boundaries. However, the rotation profile is qualitatively similar to those obtained from low  $\text{Pr}_{\text{SGS}}$  models in fully spherical shells (e.g. Brun et al. 2004; Brown et al. 2010). In Run B3, a dip at mid-latitudes is developing, which is seen to deepen in the higher  $\text{Pr}_{\text{SGS}}$  runs C3 and D3. We note that a similar transition occurs also when the density stratification is increased with  $\text{Pr}_{\text{SGS}} = 2 \dots 5$  (Käpylä et al. 2011a, 2013). The overall magnitude of the differential rotation also decreases from low to high SGS Prandtl numbers. However, much of this variation occurs already between Runs A3 and B3 whereas the differences between Runs B3, C3, and D3 are much smaller.

The time-averaged rotation profiles from runs with  $\text{Pr}_{\text{SGS}} = 1$  with varying  $\text{Pr}_M$  are shown in the lower row of Fig. 1 from Runs C2–C5. The absolute shear decreases steeply as  $\text{Pr}_M$  and  $\text{Re}_M$  increase so that in the highest  $\text{Re}_M$  case the differential rotation is appreciable only near the latitudinal boundaries. There are also qualitative changes such that the negative shear layer at mid-latitudes is almost absent in Run C5 and a near-surface shear layer is developing in Runs C4 and C5.

To quantify the radial and latitudinal differential rotation we use the quantities (Käpylä et al. 2013)

$$\Delta_{\Omega}^{(r)} = \frac{\Omega_{\text{eq}} - \Omega_{\text{bot}}}{\Omega_{\text{eq}}}, \quad \Delta_{\Omega}^{(\theta)} = \frac{\Omega_{\text{eq}} - \Omega_{\text{pole}}}{\Omega_{\text{eq}}}, \quad (26)$$

where  $\Omega_{\text{eq}} = \Omega(r_1, \pi/2)$  and  $\Omega_{\text{bot}} = \Omega(r_0, \pi/2)$  are the rotation rates at the surface and at the bottom of the convection zone at the equator. Furthermore,  $\Omega_{\text{pole}} = \frac{1}{2}[\Omega(r_1, \theta_0) + \Omega(r_1, \pi - \theta_0)]$  is the average rotation rate between the latitudinal boundaries at the outer boundary. We show  $\Delta_{\Omega}^{(r)}$  and  $\Delta_{\Omega}^{(\theta)}$  for the runs of Sets A–F in Fig. 2. We find that both radial and latitudinal differential rotation are modestly quenched for  $\text{Re}_M \lesssim 30$  in Sets A–E. For higher values of  $\text{Re}_M$ , both  $\Delta_{\Omega}^{(r)}$  and  $\Delta_{\Omega}^{(\theta)}$  decrease steeply, and for the highest values of  $\text{Re}_M$  the differential rotation is almost completely quenched. Set F with the lowest rotation rate stands apart from the other runs. The major difference in this set is that the differential rotation is anti-solar, i.e. with a slow equator and faster poles. There the radial differential rotation decreases monotonically, but the decrease is only roughly 20



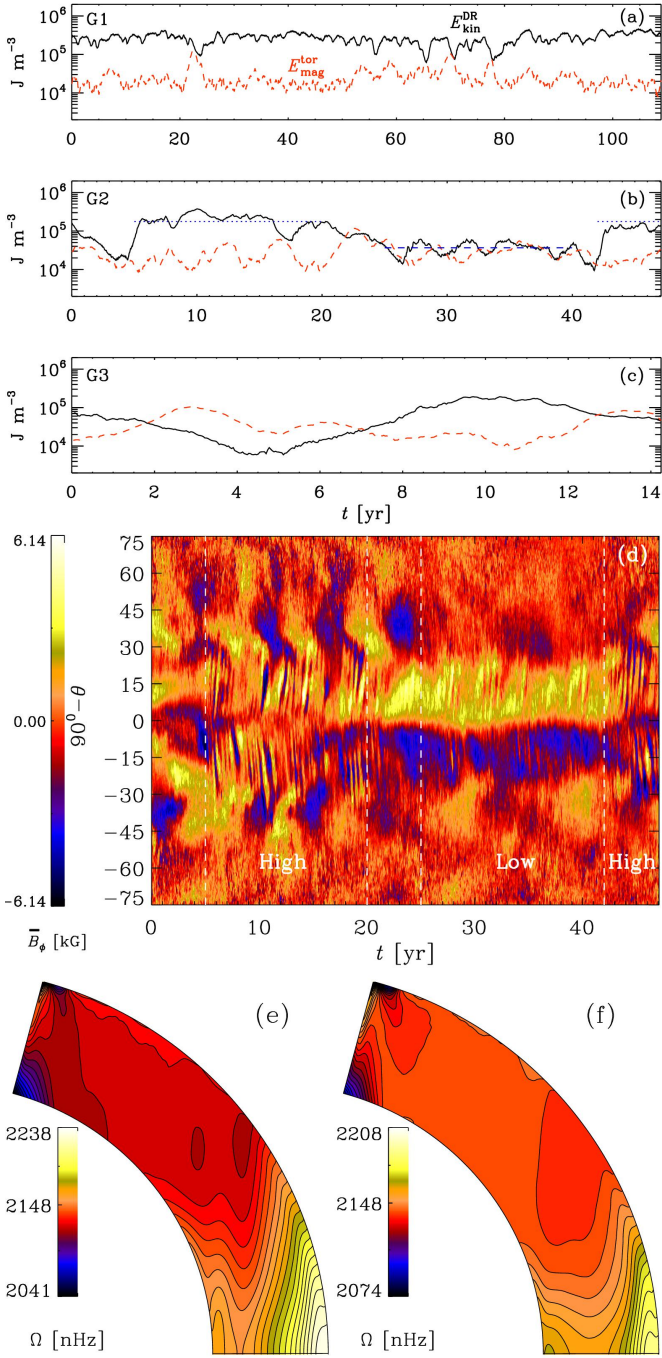


**Fig. 3.** Energies of differential rotation (black solid lines) and mean toroidal magnetic field (red dashed) as functions of time from Runs G1, G2, and G3 (panels (a)–(c)). Panel (d) shows the azimuthally averaged azimuthal magnetic field at  $r = 0.98R_{\odot}$  from Run G2. The vertical dashed lines indicate the ‘High’ and ‘Low’ states of differential rotation. Panels (e) and (f) show the time averaged rotation profiles in Run G2 from the high and low states indicated as blue dotted and dashed lines in panel (b).

per cent in the range  $Re_M = 20 \dots 151$  whereas  $\Delta_{\Omega}^{(\theta)}$  remains roughly constant above  $Re_M = 39$ . A possible explanation to the difference between Set F and the other sets is that the mean magnetic fields are stronger in the latter sets (see Table 2 and Sect. 4.2.4) leading to a stronger backreaction to the flow.

We list the kinetic energy densities of the total flow  $E_{\text{kin}} = \langle \frac{1}{2} \rho \mathbf{U}^2 \rangle_V$ , differential rotation  $E_{\text{kin}}^{\text{DR}} = \langle \frac{1}{2} \rho \overline{U_{\phi}^2} \rangle_V$ , meridional

circulation  $E_{\text{kin}}^{\text{MC}} = \langle \frac{1}{2} \rho (\overline{U_r^2} + \overline{U_{\theta}^2}) \rangle_V$ , the fluctuating velocity  $E_{\text{kin}}^{\text{fluct}} = \langle \frac{1}{2} \rho \mathbf{u}^2 \rangle_V$  and the magnetic energy densities related to the total field  $E_{\text{mag}} = \langle \overline{B^2} / 2\mu_0 \rangle_V$ , azimuthally averaged toroidal  $E_{\text{mag}}^{\text{tor}} = \langle \overline{B_{\phi}^2} / 2\mu_0 \rangle_V$  and poloidal fields  $E_{\text{mag}}^{\text{pol}} = \langle (\overline{B_r^2} + \overline{B_{\theta}^2}) / 2\mu_0 \rangle_V$ , and the fluctuating magnetic energy  $E_{\text{mag}}^{\text{fluct}} = \langle \overline{b^2} / 2\mu_0 \rangle_V$  with  $\mathbf{u} = \mathbf{U} - \overline{\mathbf{U}}$ ,  $\mathbf{b} = \mathbf{B} - \overline{\mathbf{B}}$  and where  $\langle \rangle_V$  indicates a volume average, in our simulations in Table 2. We find that the kinetic energy decreases monotonically as the magnetic Reynolds number is increased irrespective of the SGS Prandtl number. This is mostly due to quenching of the differential rotation whereas the fluctuating kinetic energy is much less affected. Differences between the sets of runs are large, however. In Set F, the total kinetic energy drops by less than a factor of two and the energy of the differential rotation by a factor of four, whereas in Sets A, B, C, and E, the  $E_{\text{kin}}$  reduces by roughly an order of magnitude and  $E_{\text{kin}}^{\text{DR}}$  by two orders of magnitude. Set D falls between the two extreme cases. The energy of the meridional flow is negligible in comparison to both differential rotation and fluctuating (non-axisymmetric) contributions.

We note, however, that the temporal variations of differential rotation increase as the magnetic Reynolds number is increased, see Table 2. This is demonstrated in Fig. 3(a)–(c) where the energies of the differential rotation and mean toroidal magnetic field are shown for Runs G1–G3. In the lowest- $Re_M$  case, both are fairly stable with  $E_{\text{mag}}^{\text{tor}}$  being typically an order of magnitude smaller than  $E_{\text{kin}}^{\text{DR}}$  with a few excursions with strong magnetic field and weak differential rotation (e.g. around  $t \approx 22$  yrs and  $t \approx 50$ – $80$  yrs). In an extended version of this run, the quiescent magnetic field leads to stronger than average differential rotation for the last 70 years of that run (see Figs. 4(a) and 4(b) of Käpylä et al. 2016a). In Run G2 with  $Re_M = 66$ , two more distinct states appear to be present: either the differential rotation is strong and the magnetic fields weak ( $t \approx 5$ – $20$  and  $t \gtrsim 42$  years) or the two are comparable ( $t \approx 25$ – $42$  years). These events are associated with a change of the large-scale dynamo mode from an oscillatory equatorward migrating mode (strong DR, weak magnetic field) to a quasi-stationary one (DR and magnetic field energies comparable), see Fig. 3(d). Panels (e) and (f) of Fig. 3 show that the latitudinal differential rotation decreases by roughly 30 per cent from the high to the low state. Similar but apparently more violent variations are seen in the highest- $Re_M$  case (Run G3), but there the time series is too short to draw solid conclusions.

Our results appear to stand apart from similar studies in full spherical shells (e.g. Nelson et al. 2013; Hotta et al. 2016) in that the differential rotation is strongly quenched as a function of the magnetic Reynolds number. However, in Nelson et al. (2013) the values of  $Rm'$  ( $= 2\pi Re_M$ ) correspond to a range of  $8 \dots 32$  in  $Re_M$  in our units where the radial and latitudinal differential rotation decrease by about 30 per cent. This is roughly consistent with our results. On the other hand, Hotta et al. (2016) reach higher values of  $Re_M$  than in the present study, but no strong quenching is reported. This can be because their models are rotating substantially slower than ours, leading to weaker magnetic fields and a weaker back reaction to the flow. Furthermore, in these models, the differential rotation is strongly influenced by their SGS heat flux, which transports one third of the luminosity. Another obvious candidate for explaining the difference is the wedge geometry used in the current simulations. However, we note that earlier simulations with a similar setup did not show a marked trend in the energy of the differential rotation as the az-

**Table 2.** Volume and time-averaged kinetic and magnetic energy densities realized in the simulations in units of  $10^5 \text{ J m}^{-3}$ .

Run	$E_{\text{kin}}$	$\delta E_{\text{kin}}$	$E_{\text{kin}}^{\text{DR}}$	$\delta E_{\text{kin}}^{\text{DR}}$	$E_{\text{kin}}^{\text{MC}}$	$\delta E_{\text{kin}}^{\text{MC}}$	$E_{\text{kin}}^{\text{fluct}}$	$\delta E_{\text{kin}}^{\text{fluct}}$	$E_{\text{mag}}$	$\delta E_{\text{mag}}$	$E_{\text{mag}}^{\text{tor}}$	$\delta E_{\text{mag}}^{\text{tor}}$	$E_{\text{mag}}^{\text{pol}}$	$\delta E_{\text{mag}}^{\text{pol}}$	$E_{\text{mag}}^{\text{fluct}}$	$\delta E_{\text{mag}}^{\text{fluct}}$
A1	12.981	0.281	12.107	0.219	0.011	0.002	0.863	0.060	0.000	0.000	0.000	0.000	0.000	0.000	0.000	0.000
A2	12.485	0.307	11.741	0.207	0.012	0.003	0.732	0.183	0.000	0.000	0.000	0.000	0.000	0.000	0.000	0.000
A3	8.067	1.150	7.362	1.133	0.009	0.000	0.695	0.017	0.293	0.023	0.197	0.019	0.011	0.002	0.086	0.011
A4	1.206	0.117	0.434	0.132	0.007	0.001	0.766	0.015	0.834	0.130	0.367	0.077	0.041	0.006	0.426	0.051
A5	1.088	0.059	0.282	0.121	0.006	0.001	0.800	0.081	1.116	0.272	0.398	0.200	0.070	0.049	0.649	0.141
B1	24.510	0.144	23.087	0.144	0.017	0.001	1.406	0.068	0.000	0.000	0.000	0.000	0.000	0.000	0.000	0.000
B2	20.505	1.056	19.036	1.028	0.015	0.001	1.454	0.033	0.680	0.021	0.350	0.021	0.041	0.003	0.289	0.007
B3	7.233	1.775	5.722	1.674	0.014	0.001	1.496	0.128	0.982	0.139	0.431	0.105	0.051	0.014	0.500	0.055
B4	1.816	0.081	0.558	0.076	0.009	0.000	1.248	0.045	1.463	0.072	0.387	0.081	0.089	0.007	0.987	0.016
B5	1.169	0.139	0.167	0.066	0.007	0.001	0.995	0.074	2.325	1.023	0.501	0.487	0.106	0.040	1.718	0.496
C1	7.248	0.364	5.695	0.359	0.014	0.000	1.538	0.011	0.000	0.000	0.000	0.000	0.000	0.000	0.000	0.000
C2	8.484	0.635	6.705	0.614	0.018	0.000	1.760	0.021	0.637	0.057	0.145	0.018	0.118	0.013	0.374	0.026
C3	4.299	0.258	2.641	0.220	0.015	0.001	1.642	0.038	1.035	0.111	0.258	0.044	0.102	0.014	0.676	0.056
C4	2.630	0.382	1.069	0.323	0.012	0.001	1.549	0.058	1.308	0.144	0.357	0.076	0.078	0.011	0.873	0.087
C5	1.310	0.062	0.156	0.041	0.007	0.000	1.146	0.063	2.138	0.071	0.309	0.074	0.089	0.008	1.740	0.121
D1	6.895	0.149	5.211	0.119	0.015	0.001	1.668	0.032	0.000	0.000	0.000	0.000	0.000	0.000	0.000	0.000
D2	6.775	0.055	4.977	0.049	0.017	0.000	1.781	0.008	0.653	0.013	0.159	0.007	0.133	0.003	0.361	0.006
D3	3.978	0.426	2.296	0.352	0.014	0.000	1.668	0.074	0.873	0.051	0.171	0.036	0.098	0.012	0.604	0.024
D4	2.012	0.130	0.545	0.110	0.010	0.000	1.457	0.020	0.987	0.041	0.145	0.039	0.074	0.003	0.768	0.026
D5	1.545	0.044	0.313	0.065	0.008	0.000	1.224	0.032	1.607	0.139	0.261	0.082	0.068	0.006	1.278	0.052
E1	26.246	0.545	23.956	0.571	0.035	0.001	2.255	0.066	0.366	0.013	0.107	0.008	0.027	0.002	0.232	0.017
E2	3.904	1.355	1.881	1.289	0.022	0.002	2.000	0.064	1.252	0.137	0.424	0.102	0.070	0.011	0.758	0.064
E3	2.236	0.336	0.542	0.265	0.017	0.001	1.677	0.069	1.377	0.142	0.235	0.064	0.074	0.006	1.068	0.087
E4	2.170	0.114	0.428	0.151	0.017	0.000	1.724	0.056	1.700	0.118	0.267	0.068	0.061	0.007	1.372	0.075
F1	7.383	2.069	4.140	2.086	0.119	0.006	3.124	0.141	0.836	0.106	0.154	0.038	0.101	0.039	0.581	0.095
F2	4.845	0.094	1.524	0.147	0.099	0.002	3.222	0.055	0.871	0.055	0.083	0.002	0.063	0.017	0.724	0.038
F3	4.432	0.111	1.307	0.028	0.086	0.002	3.039	0.093	0.910	0.088	0.067	0.009	0.042	0.012	0.801	0.066
F4	4.015	0.095	1.057	0.092	0.079	0.001	2.880	0.016	1.177	0.050	0.061	0.004	0.036	0.004	1.079	0.041
G1	4.299	0.258	2.641	0.220	0.015	0.001	1.642	0.038	1.035	0.111	0.258	0.044	0.102	0.014	0.676	0.056
G2	2.782	0.947	1.026	0.680	0.014	0.003	1.742	0.264	1.501	0.233	0.288	0.086	0.090	0.008	1.123	0.161
G3	2.401	0.608	0.654	0.487	0.014	0.002	1.733	0.224	1.938	0.212	0.372	0.122	0.087	0.034	1.479	0.124

**Notes.** Runs A1, A2, B1, C1, and D1 do not have dynamos. The  $\delta$ -quantities represent the variations in time. These are computed by first dividing the time series in three equally long parts and temporally averaging over each of these. Then the greatest deviation of these quantities from the average over the whole time series is taken to represent the variations in time.

imuthal extent of the domain was varied (see Table 1 of Käpylä et al. 2013). However, results of Boussinesq simulations of convective dynamos have shown a similar change as a function of the magnetic Prandtl number (Schrinner et al. 2012). The drop in the amplitude of the differential rotation was associated with a change in the dynamo mode from an oscillatory multipolar solution to a quasi-steady dipolar configuration (cf. Fig. 15 of Schrinner et al. 2012) that prevents strong differential rotation from developing. We do not find a strong dipole component in our simulations (see, Sect. 4.2.3). However, the strong suppression of the differential rotation often coincides with the appearance of a small-scale dynamo (see Table 1 and the discussion in the Sect. 4.1.2) or a change in the large-scale dynamo mode as discussed above.

#### 4.1.2. Angular momentum transport

The azimuthally averaged  $z$ -component of the angular momentum is governed by the equation:

$$\frac{\partial}{\partial t}(\bar{\rho}\varpi^2\Omega) + \nabla \cdot \{ \varpi[\varpi\bar{\rho}\bar{U}\Omega + \bar{\rho}\bar{u}_\phi\bar{\mathbf{u}} - 2\nu\bar{\rho}\bar{\mathbf{S}} \cdot \hat{\phi} - \mu_0^{-1}(\bar{B}_\phi\bar{\mathbf{B}} + \bar{b}_\phi\bar{\mathbf{b}})] \} = 0, \quad (27)$$

where  $\varpi = r \sin \theta$  is the lever arm and velocity and magnetic field have been decomposed into mean and fluctuating parts according to  $U_i = \bar{U}_i + u_i$  and  $B_i = \bar{B}_i + b_i$ . We will denote the Reynolds and Maxwell stresses as  $Q_{ij} = \bar{u}_i\bar{u}_j$  and  $\mathcal{M}_{ij} = -\bar{b}_i\bar{b}_j/\mu_0\bar{\rho}$ , respectively. Note that Eq. (27) differs from the formulation of, e.g., Brun et al. (2004) in that we have retained terms containing the mass flux  $\rho\bar{U}$  in the contributions corresponding to the meridional circulation. This is because in our fully compressible setup,  $\nabla \cdot \rho\bar{U}$  is non-zero. This is particularly important for the average radial mass flux  $\bar{\rho}\bar{U}_r$ . However, we found that the effects of compressibility in the Reynolds stress and the viscous terms are negligible<sup>2</sup>.

The main generator of differential rotation is commonly thought to be the Reynolds stress and in particular its non-diffusive contribution due to the  $\Lambda$  effect (Rüdiger 1980, 1989). Disentangling the contributions from the  $\Lambda$  effect and the turbulent viscosity is currently only possible using assumptions regarding either of the two coefficients and computing the other from the Reynolds stress (e.g. Käpylä et al. 2014; Karak et al. 2015; Warnecke et al. 2016a). We will not attempt this here but study the total turbulent stress  $T_{ij} = Q_{ij} + \mathcal{M}_{ij}$  and the anisotropy parameters realized in simulations with varying

<sup>2</sup> This means that terms of the form  $(\rho u_i)'u_j$ , where the prime denotes fluctuations,  $\bar{\rho}u_i u_j$ , and  $\nu\bar{\rho}u_i u_j$  are neglected.



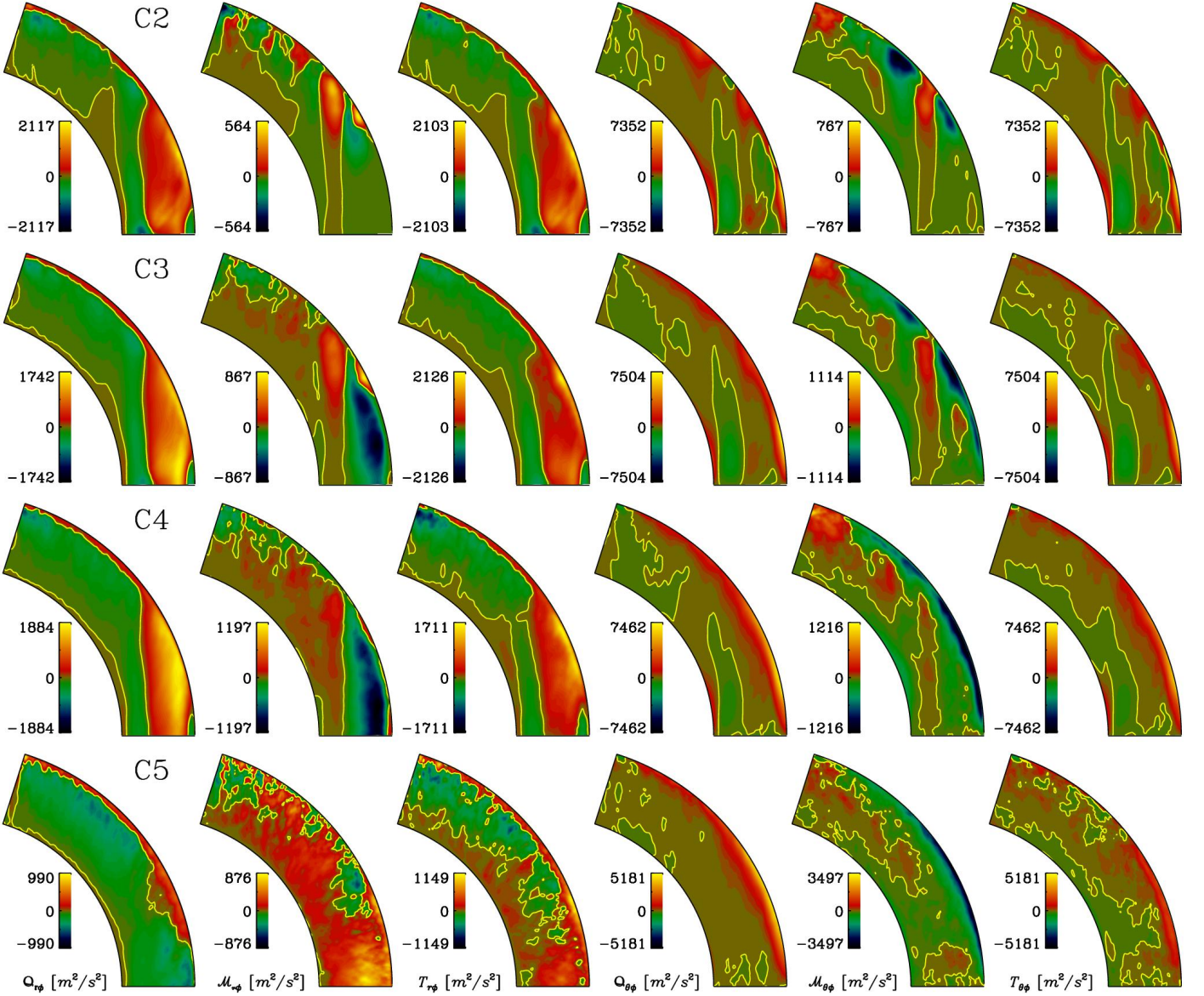


**Fig. 4.** From left to right: Reynolds, Maxwell, and total stress components  $\mathcal{Q}_{r\phi}$ ,  $\mathcal{M}_{r\phi}$ ,  $T_{r\phi}$ ,  $\mathcal{Q}_{\theta\phi}$ ,  $\mathcal{M}_{\theta\phi}$ , and  $T_{\theta\phi}$  for Runs C2 (top), C3, C4, and C5 (bottom). Data nearer than  $2.5^\circ$  from the latitudinal boundaries are not shown, so as to emphasize the structures at lower latitudes. The yellow contours denote the zero levels in each panel.

magnetic Reynolds number. Figure 4 shows the off-diagonal Reynolds stress components,  $\mathcal{Q}_{r\phi}$  and  $\mathcal{Q}_{\theta\phi}$ , from Runs C2 to C5 with  $\text{Re}_M$  varying between 14 and 146. The spatial structures of both stress components remain relatively similar in Runs C2, C3, and C4. Neither of the stresses show a monotonous behavior as functions of  $\text{Re}_M$ , both being generally smaller in Run C3 in comparison to Runs C2 and C4. However, in Run C5 the overall magnitude is decreased by a factor of two for  $\mathcal{Q}_{r\phi}$  and about 15 per cent for  $\mathcal{Q}_{\theta\phi}$ . No corresponding decrease is observed in the diagonal components of the stress, whose overall magnitude is given by the fluid Reynolds number; see Table 1.

We find that for magnetic Reynolds numbers up to roughly 30, the off-diagonal Maxwell stresses are smaller than the corresponding Reynolds stresses. The magnitude of the vertical component  $\mathcal{M}_{r\phi}$  is between a quarter and a half of  $\mathcal{R}_{r\phi}$ , whereas for the horizontal component the difference is greater. With higher  $\text{Re}_M$ , the Maxwell stresses attain similar profiles as the Reynolds

stresses but with opposite signs. The magnitudes of the Maxwell stresses increase with  $\text{Re}_M$  such that they become comparable to and locally even larger than the Reynolds stresses at the highest magnetic Reynolds numbers. The total vertical stress  $T_{r\phi}$  decreases for Runs C2–C4 such that the effect is most clear near the equator. For Run C5 the vertical stress is dominated by the Maxwell stress near the equator. The horizontal component  $T_{\theta\phi}$  decreases monotonically as  $\text{Re}_M$  increases. The near cancellation of the total stress at high  $\text{Re}_M$  is likely to contribute significantly to the quenching of differential rotation. These results are apparently at odds with those of Karak et al. (2015) who reported that the Maxwell stress is an order of magnitude smaller than the Reynolds stress. However, their simulations were in a regime near the transition between anti-solar and solar-like rotation profiles with relatively weak and intermittent large-scale dynamos.

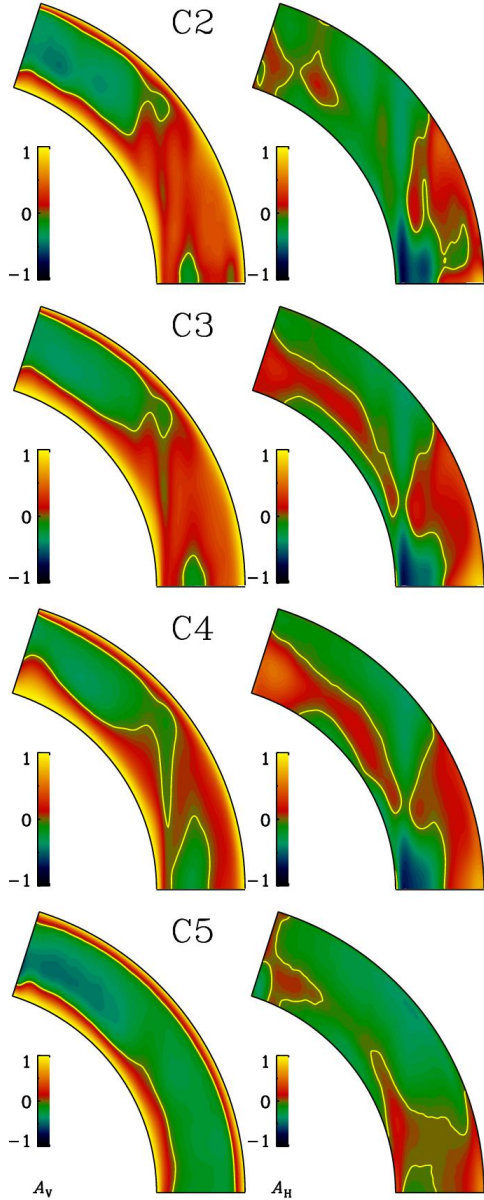


**Fig. 5.** Anisotropy parameters  $A_V$  (left) and  $A_H$  (right) for the same runs as in Fig. 4. The yellow contours denote the zero levels in each panel.

In Set F with anti-solar differential rotation the Reynolds stresses show only a weak decreasing trend as a function of  $Re_M$  with a corresponding increase in the Maxwell stress (not shown). The vertical Maxwell stress has an opposite sign in comparison to the Reynolds stress in all cases while a similar tendency for the horizontal stress is not so clear. The magnitude of the vertical Maxwell stress is roughly half of the corresponding Reynolds stress while the amplitude of the horizontal Maxwell stress is significantly weaker than the horizontal Reynolds stress. The much weaker quenching of the total turbulent stress in Set F is consistent with a clearly milder decrease of the differential rotation than in the other sets.

Assuming that the turbulent viscosity follows a naive mixing length estimate, the quenching of the differential rotation can indicate that the  $\Lambda$  effect is more severely quenched by the large-scale magnetic field at high magnetic Reynolds numbers.

Another possibility is that small-scale magnetic fields generated by an efficient small-scale dynamo contribute to enhancing the turbulent viscosity. In a recent paper, Hotta et al. (2016) suggest that the small-scale dynamo at high  $Re_M$  suppresses velocity at small scales, and facilitates the growth of the large-scale magnetic fields. First-order smoothing estimates for isotropic and homogeneous turbulence (M. Rheinhardt, private communication) suggest that turbulent viscosity acquires a contribution  $\nu_t^{(SSD)} = \frac{1}{3} b_{rms}^{(0)} k_f^{-1}$ , where  $b_{rms}^{(0)}$  is the rms-value of the saturated fluctuating magnetic field due to small-scale dynamo. We find that the fluctuating magnetic field energy grows monotonically as a function of  $Re_M$ ; see Table 2. A corresponding increase of turbulent viscosity would be compatible with a strong decrease of differential rotation. However, we find two counterexamples: in Set A, no SSD is present but the differential rotation still experiences strong quenching, and in Set F, an SSD is present but differential rotation remains strong. Furthermore, the dependence of the  $\Lambda$  effect on small-scale magnetic fields is currently unknown. Thus the question of the effect of small-scale dynamo on the turbulent transport of angular momentum at large scales remains open.

We also show the anisotropy parameters (Fig. 5)

$$A_V = \frac{Q_{\phi\phi} - Q_{rr}}{Q_{\phi\phi} + Q_{rr}}, \quad (28)$$

$$A_H = \frac{Q_{\phi\phi} - Q_{\theta\theta}}{Q_{\phi\phi} + Q_{\theta\theta}}, \quad (29)$$

which are proportional respectively to the vertical and horizontal  $\Lambda$  effects in mean-field hydrodynamics (Rüdiger 1980) under the assumption of slow rotation (see also the numerical results of Käpylä & Brandenburg 2008). Again the differences between Runs C2 and C3 are relatively small, whereas in Runs C4 and C5 the mostly positive  $A_V$  at mid-latitudes in lower- $Re_M$  runs gives way to negative values. According to mean-field theory, this corresponds to a sign change of the vertical  $\Lambda$  effect that is responsible for generating radial differential rotation (Rüdiger 1980). The magnitude and the spatial distribution of the horizontal anisotropy parameter  $A_H$  are significantly different in Run C5 in comparison to the other runs whereas the differences between the other runs are less significant. The negative values of  $A_H$  at mid-latitudes in Runs C2–C4 coincide with the minimum in the angular velocity suggesting that the horizontal  $\Lambda$  effect is negative there. In Run C5 the overall magnitude of  $A_H$  is diminished near the surface at low latitudes. Along with the change of sign of  $A_V$  this is likely to contribute to the reduced differential rotation as a function of  $Re_M$ . However, more theoretical work is needed to disentangle the effects of the small- and large-scale magnetic fields on the angular momentum transport.

The discussion above is valid, if the angular momentum is in a statistically steady state demanding that the sum of two terms,  $\text{div}F_r + \text{div}F_\theta$ , vanishes, i.e.,

$$\frac{1}{r^2} \frac{\partial(r^2 F_r)}{\partial r} + \frac{1}{r \sin \theta} \frac{\partial(\sin \theta F_\theta)}{\partial \theta} \equiv \text{div}F_r + \text{div}F_\theta = 0, \quad (30)$$

where

$$F_r = \varpi \left[ \varpi \overline{\rho U_r} \Omega + \overline{\rho} Q_{r\phi} - \nu \rho \varpi \frac{\partial \Omega}{\partial r} - \mu_0^{-1} (\overline{B_\phi B_r} + \overline{b_r b_\phi}) \right], \quad (31)$$

and

$$F_\theta = \varpi \left[ \varpi \overline{\rho U_\theta} \Omega + \overline{\rho} Q_{\theta\phi} - \nu \rho \frac{\varpi}{r} \frac{\partial \Omega}{\partial \theta} - \mu_0^{-1} (\overline{B_\phi B_\theta} + \overline{b_\theta b_\phi}) \right]. \quad (32)$$



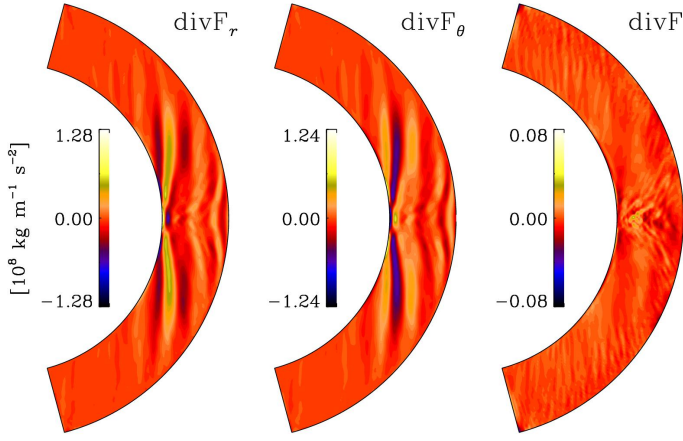


**Fig. 6.** Radial ( $\text{div}F_r$ , *left panel*) and latitudinal ( $\text{div}F_\theta$ , *middle*) parts of the divergence of the angular momentum fluxes. The *right panel* shows the total divergence. The units are given in the legend. Data taken from Run C3.

Figure 6 shows representative results from Run C3 for the terms  $\text{div}F_r$  and  $\text{div}F_\theta$ , as well as their sum. We find that the radial and latitudinal contributions have similar structures but opposite signs and that their sum is at most roughly seven per cent of the individual components. The elongated structures at low latitudes within the tangent cylinder are due to the meridional circulation which yields the dominant contribution to the divergence. We note that neither the radial nor the latitudinal fluxes need to individually cancel for the divergence to vanish.

## 4.2. Large-scale magnetic fields and dynamo cycles

### 4.2.1. General considerations

We find no dynamos in the lowest magnetic Reynolds number cases Runs A1, A2, B1, C1, and D1 which are in the range  $\text{Re}_M = 5 \dots 9$ . On the other hand, the highest magnetic Reynolds numbers clearly exceed critical values for small-scale dynamo action to occur in simpler setups (e.g. Schekochihin et al. 2005). In the present simulations the small- and large-scale dynamos can be excited at the same time and disentangling the two is not directly possible. Thus we resort to runs where we artificially suppress the large-scale ( $\phi$ -averaged) magnetic fields at each time step. This eliminates the large-scale dynamo and growing magnetic fields can be associated with a small-scale dynamo. We have performed such runs for each of the cases where a dynamo is observed and find that a small-scale dynamo is excited in Runs B5, C5, D4, D5, E3, E4, F4, G2, and G3.

### 4.2.2. Cycle detection using $D^2$ analysis

Using the  $D^2$  statistic discussed in Sect. 3, we analyzed separately radial and azimuthal components of the mean magnetic field. In the former case we included all the data near the polar region ( $55^\circ \leq |90^\circ - \theta| \leq 75^\circ$ ) and in the latter case data around mid-latitude region ( $10^\circ \leq |90^\circ - \theta| \leq 45^\circ$ ). We considered data above  $0.94R_\odot$  and analyzed the northern and southern hemispheres separately.

The results of the analysis are listed in Table 3. We required that at least five full cycles were covered for each trial period in the period search range. To meet this criteria we adjusted the upper limit of the period search range according to the length of

**Table 3.** Cycle lengths detected using  $D^2$  statistic.

Run	$P^{\max}$	$l_{\text{coh}}^{\max}$	Cycle length				Class
			$\overline{B}_\phi(\text{N})$	$\overline{B}_\phi(\text{S})$	$\overline{B}_r(\text{N})$	$\overline{B}_r(\text{S})$	
A3	11	5	4.06	—	3.71	—	PW
A4	7	5	—	5.31	—	—	PW
A5	5	5	—	—	—	—	(QS/IR)
B2	5	5	1.57	1.42	2.29	1.92	PW
B3	5	5	—	—	4.57	4.77	IR
B4	10	5	8.14	—	9.16	—	IR
B5	5	5	—	—	4.90	4.90	(PW)
C2	7	6	3.40	3.34	3.40	3.34	EW
C3	21	5	5.11	5.24	4.99	5.11	EW
C4	13	5	—	7.30	8.81	7.56	EW
C5	7	5	—	—	—	6.80	(QS/IR)
D2	6	9	3.44	3.39	3.44	3.39	EW
D3	12	5	5.85	5.27	5.70	5.14	EW
D4	8	5	—	—	—	—	(EW)
D5	5	5	—	—	—	—	(QS/IR)
E1	2	5	1.66	1.50	1.70	—	PW
E2	11	5	5.89	6.05	6.23	6.05	IR
E3	14	5	8.46	6.42	8.81	6.05	(QS/IR)
E4	4	5	—	—	—	—	(QS/IR)
G2	10	5	5.96	—	6.30(9.57)	9.57(6.48)	EW/QS

**Notes.** Here  $P^{\max}$  and  $l_{\text{coh}}^{\max}$  are the upper limit for the period search range and the maximum coherence length, respectively. They are related via  $\Delta t \approx P^{\max} l_{\text{coh}}^{\max}$ . Values in the fourth to seventh columns are detected cycle periods (in years) for azimuthal ( $\overline{B}_\phi$ ) and radial ( $\overline{B}_r$ ) mean magnetic fields in north (N) and south (S) hemispheres. “—” stands for no detection. The last column indicates the classification of the dynamo solution, see Sect. 4.2.3. Brackets indicate an uncertain classification due to too short time series.

the dataset, while the lower limit was always fixed at one year. We set the lower limit for the coherence length range to two cycles per given period and the upper value was determined by the dataset length. However, in some cases the longest possible trial period was still below two years in which cases the analysis was deemed infeasible. This situation was encountered for Run G3, which has therefore not been included in Table 3. Furthermore, Runs A1, A2, B1, C1, and D1 without dynamos were not analysed.

All the cycle lengths given in the table are significant with the p-values less than 1%. More precisely, in our case the p-value represents a probability that a cycle with a given period would appear by chance out of white noise data with the same distribution as the original data. In those cases where the obtained  $D^2$  spectrum contained no significant minima, no cycle was detected. However, here we must also note that due to the narrowing of the period search range in some cases it is possible that the real cycle length is located outside the range and we did not detect it. This is particularly relevant for the runs at high magnetic Reynolds numbers where the time series are short.

In all the sets, especially if one leaves out the highest Reynolds number cases, the cycle lengths are found to increase as functions of the magnetic Prandtl number. Thus, the dynamo period is sensitive to the strength of the magnetic diffusion such that when the diffusion is decreased, and correspondingly the diffusion time scale increases, the dynamo period gets longer.

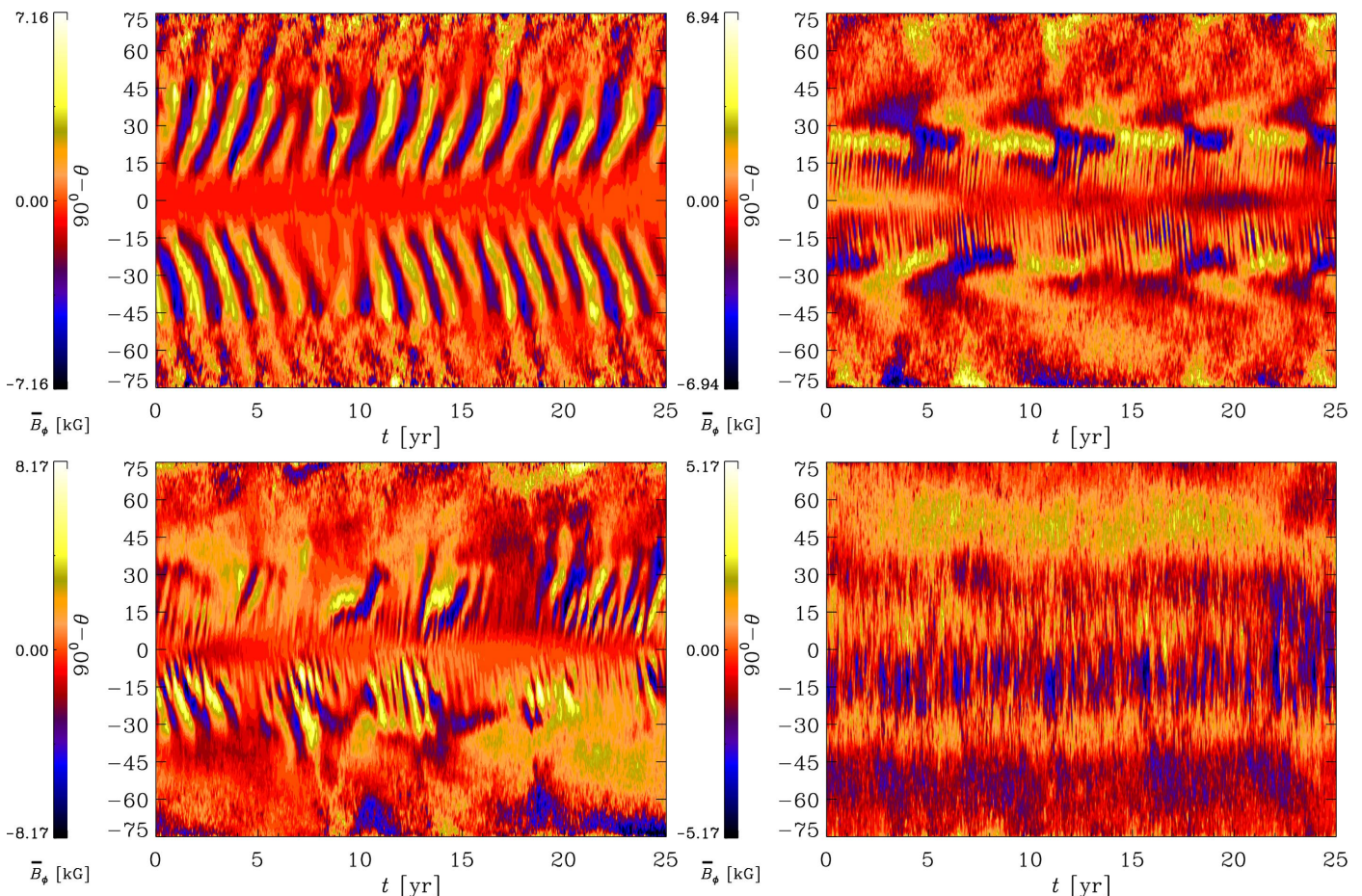


**Fig. 7.** Azimuthally averaged azimuthal magnetic field near the surface from Runs B2 (*top left*), D3 (*top right*), B3 (*bottom left*), and F3 (*bottom right*) with poleward (PW), equatorward (EW), irregular (IR), and quasi-stationary (QS) dynamo solutions, respectively.

#### 4.2.3. Dynamo modes

Given that recent simulations reproduce solar-like magnetic cycles with equatorward migration (hereafter EW) of activity belts, it is of interest to probe the parameter space to determine when such solutions are excited. Having identified cyclic solutions with the  $D^2$  statistics we classify them as EW or PW (poleward) based on the migration direction of the dynamo wave at low latitudes between  $\pm 10^\circ$  and  $\pm 45^\circ$ . We also find quasi-stationary (hereafter QS) solutions in Set F. If a clear classification by visual inspection cannot be made we classify the solution as irregular (IR). In some cases features from more than one class can be present, e.g. an equatorward cyclic variation on top of a quasi-stationary background. This solution is classified as EW/QS but typically such cases are quite uncertain and are indicated by brackets in the last column of Table 3. No large-scale dynamo action is denoted by ND. In Fig. 7 we show time-latitude plots of the azimuthally averaged azimuthal magnetic field  $\bar{B}_\phi$  from four runs exemplifying each of the main dynamo modes discussed above.

We first consider the Sets A–D with  $\Omega_0 = 5\Omega_\odot$ . For  $\text{Pr}_{\text{SGS}} = 0.25$  (Set A) and moderate  $\text{Re}_M$  we obtain solutions with clear poleward migration. This type of dynamos were first obtained already in the pioneering studies of Gilman (1983) and Glatzmaier (1985). Solutions showing poleward migration have been reported more recently by many groups (e.g. Käpylä et al. 2010b; Brown et al. 2011; Schrunner et al. 2012). In one case

(Run A3) we see a hemispheric dynamo with poleward migration, similar to those reported by e.g. Busse (2002) and Gastine et al. (2012). In the largest  $\text{Re}_M$  case (Run A5) the clear oscillatory solutions of the runs with smaller Reynolds numbers give way to possibly irregularly reversing or quasi-stationary large-scale fields. The time series is too short, however, for possible cycles to be detected. For  $\text{Pr}_{\text{SGS}} = 0.5$  (Set B) we find a PW mode excited in the case  $\text{Re}_M = 12$  (Run B2). At intermediate  $\text{Re}_M$  (Runs B3 and B4) the solutions mostly show irregularly reversing fields, although features from both PW and EW modes can be discerned at times; see the lower left panel of Fig. 7. The highest Reynolds number case (Run B5) appears to return to a poleward oscillatory mode with a longer cycle period. However, the large-scale field shows only four reversals in the 24 year duration of the simulation and the  $D^2$  statistic captures this only in one of the four analyzed cases. Therefore the classification of this run as PW is deemed less robust than those of the other runs in this set.

For  $\text{Pr}_{\text{SGS}} \geq 1$  (Sets C and D) we often find solutions with EW migration (Runs C2, C3, D2, D3, and D4). In Run D4 the solution is clearly EW but the time series covers only three full cycles and is thus not detected by  $D^2$ . The transition from poleward migrating to equatorward migrating solutions at intermediate magnetic Reynolds numbers coincides with the change of the rotation profile from runs with consistently positive radial gradient of  $\Omega$  to ones with a minimum of  $\Omega$  at mid-latitudes where  $\partial\Omega/\partial r < 0$  as  $\text{Pr}_{\text{SGS}}$  increases. The change in the dy-



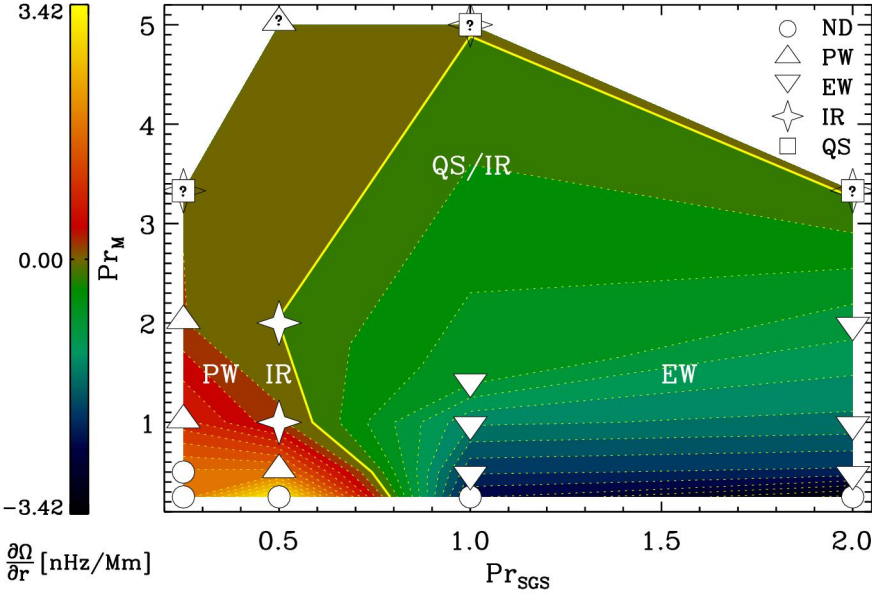


**Fig. 9.** Colour contours: radial derivative of  $\Omega$  at  $r = 0.85R_{\odot}$  averaged from latitudes  $+25^{\circ}$  and  $-25^{\circ}$ . The dynamo modes realized in Sets A–D are overplotted with abbreviations ND, PW, EW, IR, and QS. The thick yellow curve indicates the zero level of  $\partial\Omega/\partial r$ . Overlapping symbols denote solutions that show characteristics from several modes while question marks indicate that the classification is uncertain due to insufficient length of the data set.

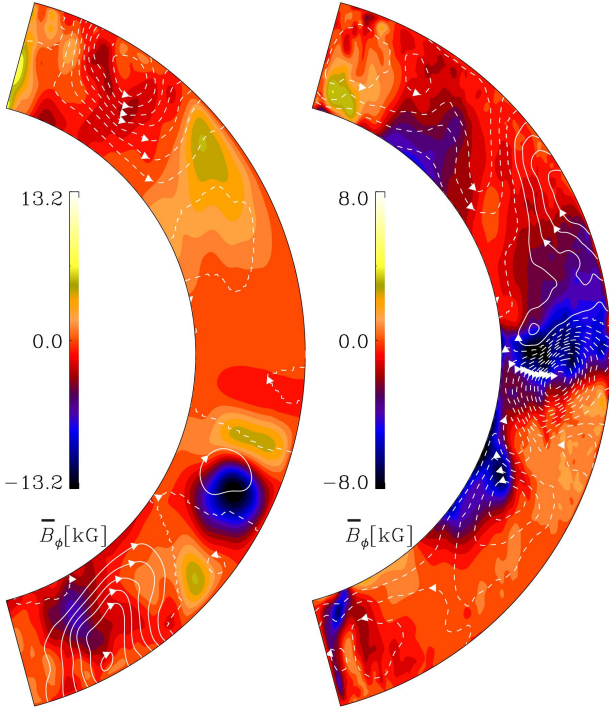


**Fig. 8.** Azimuthally averaged azimuthal magnetic field  $\bar{B}_{\phi}$  (colour contours) in units of kG and the fields lines of the poloidal field (continuous and broken lines for clockwise and anticlockwise loops, respectively). *Left:* Data from Run B2 averaged over three months near a cycle maximum at  $t = 70$  years. *Right:* Data from Run A5 averaged over the last 10 years of the run.

namo mode fits with the interpretation in terms of a classical dynamo wave obeying the Parker–Yoshimura rule (Warnecke et al. 2014, 2016b). For the highest magnetic Reynolds number cases in Sets C and D we again observe possibly quasi-stationary or irregular configurations. This classification is based on significantly shorter time series than in the other cases and it is possible that there are cycles that are much longer than

in the low- $Re_M$  cases or that a prolonged transient is still in progress. These results appear to be in agreement with those of Schinnerer et al. (2012) who found a transition from oscillatory dynamos to non-oscillatory ones at a roughly comparable  $Re_M$  for Boussinesq convection in spherical shells. They also showed that in the high- $Pr_M$  regime the two bistable branches of dynamo solutions merge and that only strongly dipolar dynamos with weak differential rotation survive. However, Gastine et al. (2012) have shown that for sufficiently density stratified cases the dipolar branch does not exist at least for moderate values of  $Re_M$ . Our simulations with moderate density stratification of  $H_{\rho} \approx 3$ , where  $H_{\rho} = -(\partial \ln \rho / \partial r)^{-1}$  is the density scale height, do not indicate that a dipolar mode takes over high  $Re_M$ , see Fig. 8 for a representative result from Run A5. This is consistent with the results of Gastine et al. (2012) who found no dipole-dominated dynamos for  $H_{\rho} \gtrsim 2$ .

The realized solutions from the runs in Sets A–D are plotted in the  $(Pr_{SGS}, Pr_M)$ -plane in Fig. 9. We find that the low and intermediate  $Re_M$  runs produce cyclic solutions with PW for low  $Pr_{SGS}$  and EW for high  $Pr_{SGS}$ . The case  $Pr_{SGS} = 0.5$  works as a watershed between the two cyclic regimes. The dynamos at high  $Re_M$  are fundamentally different from their more diffusive counterparts in that the differential rotation is almost absent. Although the ratio of the energies in the mean poloidal to toroidal components is not significantly different in the high- $Re_M$  runs in comparison to lower- $Re_M$  runs in each set, the dynamos at the high- $Re_M$  regime can be of  $\alpha^2$  type. Substantiating this claim, however, requires that the turbulent transport coefficients relevant for the maintenance of large-scale magnetic fields are extracted from the simulations and applied in corresponding mean-field models which is not within the scope of the present study.

In Set E we find a PW solution for the lowest  $Re_M$  (Run E1) whereas at higher  $Re_M$  we find IR (E2) and irregular/quasi-stationary (E3 and E4) configurations. Generally, Set E behaves similarly as Sets A–C, i.e. a transition from oscillatory dynamos at intermediate  $Re_M$  to quasi-stationary or irregularly varying solutions at high  $Re_M$ . However, Run B1 of Warnecke et al. (2016a) is similar to Run E2, but with  $Pr_{SGS} = 2$  instead of 1 shows EW. Set F is qualitatively different from the other sets similarly as for the differential rotation. The large-scale mag-



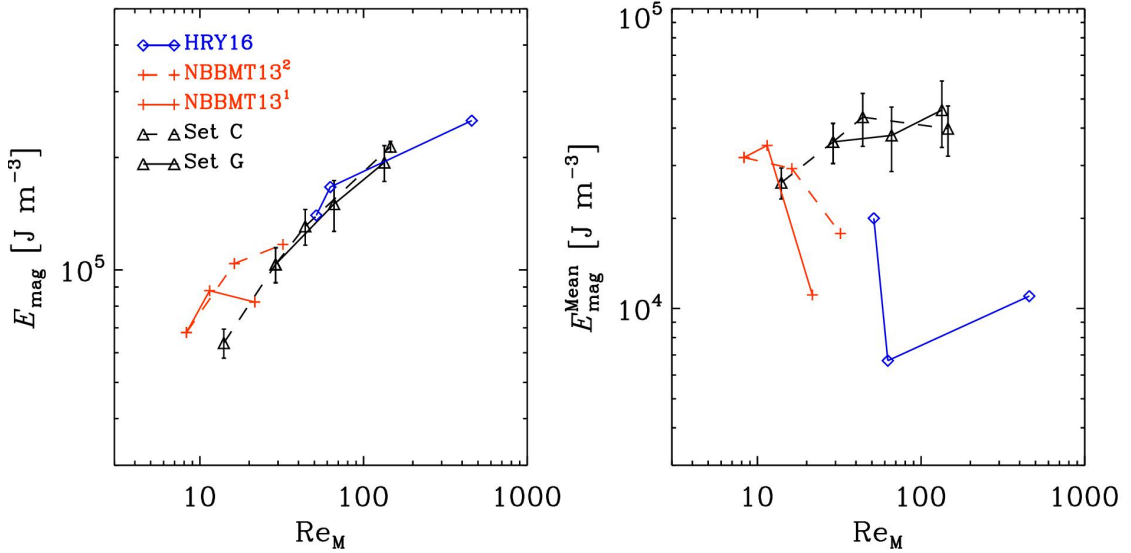


**Fig. 10.** Energy densities of the total magnetic field (*left panel*), and the azimuthally averaged fields (*right*) from Sets C (black dashed line) and G (black solid), from two sets of runs by Nelson et al. (2013) (solid and dashed red lines) and from Hotta et al. (2016) (blue solid lines). The red solid line consists of data from Cases D3, D3a, and D3b of Nelson et al. (2013) with  $\text{Pr}_M = \text{const} = 0.5$ . Correspondingly, the dashed red line shows data from Cases D3, D3-pm1, and D3-pm2 of Nelson et al. (2013) with  $\text{Pr}_M$  varying from 0.5 to 2. From Hotta et al. (2016) we show data for Cases ‘Low’, ‘Medium’, and ‘High’.

netic fields show a quasi-stationary configuration in all of the runs in Set F. In Run G2 the modulation of the differential rotation was shown to be related to a changing large-scale dynamo mode that is either EW or QS; see panels (b) and (d) of Fig. 3. In the highest- $\text{Re}_M$  case, Run G3, the two competing modes appear to be present again, but the short data set length renders such classifications preliminary at best.

#### 4.2.4. Saturation level of large-scale magnetic fields

For the total magnetic energy we find a monotonically increasing trend as a function of  $\text{Re}_M$  in all sets, see representative results in the left panel of Fig. 10 and Table 2. The absolute value of the axisymmetric parts of the poloidal and toroidal magnetic fields shows monotonically decreasing trends only in Set F with antisolar differential rotation. In the other sets the energies of the poloidal and toroidal mean fields typically do not behave monotonically as functions of  $\text{Re}_M$ . However, given the large temporal variations, our results are compatible with mean magnetic field energies converging to constant values at high magnetic Reynolds numbers, see the right panel of Fig. 10 for the results of Sets C and G. The same conclusion applies also to Set F. The findings for the mean magnetic fields appear to be in contradiction with the results of Nelson et al. (2013) who found a monotonically decreasing trend as a function of  $\text{Re}_M$ ; see Fig. 10.

The main difference to the simulations of Nelson et al. (2013) is that their models were done with a full spherical shell as opposed to the wedge geometry used here, and that magnetic field boundary condition at the outer radial boundary uses extrapolation to a potential field rather than a radial field condition as in the present study. Furthermore, Nelson et al. (2013) consider anelastic models whereas in our case the gas is fully compressible. Simulations with forced turbulence in spherical shells with coronal envelopes have shown that a higher field strength can be achieved, if the magnetic field at the boundary is not restricted to being purely radial (Warnecke & Brandenburg 2014). Furthermore, Nelson et al. (2013) use profiles for  $\nu$  and  $\eta$  which are absent in our study. The constant diffusion coefficients used

here may lead to a steeper increase of the magnetic field energy than in the runs of Nelson et al. (2013) where the local value of  $\text{Re}_M$  is significantly higher in the deeper layers. Detailed comparisons of diffusion schemes and parameter values are presented in Tables A.1 and A.2 in Appendix A.

It is difficult to assess which of these differences is the most important. However, a plausible candidate is the change of topology of the field in the full-sphere simulations of Nelson et al. (2013). As described in Käpylä et al. (2013), the large-scale magnetic field can become dominated by low-order non-axisymmetric modes and therefore applying an axisymmetric mean will average out such field contributions (see their Fig. 16 and Table 2). Evidence of such non-axisymmetric modes can be seen in the instantaneous magnetic fields in Figs. 4 and 6 of Nelson et al. (2013). However, it is not possible to assess how the degree of non-axisymmetry behaves as a function of  $\text{Re}_M$  in the results of Nelson et al. (2013) and thus a direct comparison is not possible.

In another recent study, Hotta et al. (2016) present results from less rapidly rotating ( $\Omega = \Omega_\odot$ ) simulations at high values of  $\text{Re}_M$ . Such simulations are less likely to contain significant non-axisymmetric modes. Their main claim is that whereas the mean magnetic energy decreases at intermediate  $\text{Re}_M$ , it recovers as  $\text{Re}_M$  is increased further. We have included their results in Fig. 10 for comparison. However, only a rough comparison is possible as only three data points are available and a jump occurs between the two lowest- $\text{Re}_M$  runs which is caused by a switch from explicit diffusion to a numerical slope-limited scheme. The absolute values for the mean fields are also lower than ours likely because their large-scale dynamo is less efficient than in the present study due to their slower rotation. Thus only the trend as a function of  $\text{Re}_M$  can be compared with the current results or with those of Nelson et al. (2013). The results of Hotta et al. (2016) are more in line with ours, but the degree of temporal variations is indicated only in passing<sup>3</sup> and it is not possible

<sup>3</sup> Hotta et al. (2016) state that during the last 200 days the mean magnetic field energy in the simulation ‘High’ is almost 2.5 times higher

to assess the steepness of the increasing trend of the energy of the mean field as a function of  $Re_M$  accurately.

## 5. Conclusions

We find that, as the SGS Prandtl number (responsible for sub-grid scale turbulent transport) is increased, the rotation profiles realized in the simulations develop a region of negative shear at mid-latitudes. At moderate  $Re_M$  this latitude coincides with a transition from poleward migrating to equatorward migrating dynamo modes. This can be explained by interpreting the solutions as dynamo waves propagating along the isocontours of constant shear (Parker 1955; Yoshimura 1975). However, it appears that, as  $Pr_M$  is sufficiently high (corresponding to high  $Re_M$ ), the regular cycles give way to quasi-stationary or irregularly varying solutions. However, due to computational constraints, the time series of these runs are typically significantly shorter than of the lower- $Re_M$  runs, so cyclic solutions with long cycle periods cannot be ruled out.

We also find that the cycle length of the dynamo solution undergoes a systematic increase when the magnetic Prandtl number is increased: seemingly independent of the other parameters, the decreasing magnetic diffusivity leads to longer cycles. The highest Reynolds number runs are, however, too short for our period analysis to work conclusively.

We find a strong dependence of the differential rotation on the magnetic Reynolds number so that for the highest values of  $Re_M$  both radial and latitudinal shear are almost absent. The strongest quenching tends to appear in cases where a small-scale dynamo is present. However, there are exceptions. The physical reason for the quenching is therefore unclear, but several mechanisms appear plausible. First, the small-scale magnetic field can enhance turbulent viscosity or quench the  $\Lambda$ -effect responsible for maintaining differential rotation. Suppression of *small-scale* flows due to the small-scale magnetic fields has been suggested by Hotta et al. (2016). We find that at intermediate  $Re_M$ , the Maxwell stress is of the same order of magnitude as the Reynolds stress and becomes comparable at high  $Re_M$ . Because of their opposite signs, the total stress is diminished. We expect that for intermediate and in particular for high  $Re_M$ , the Maxwell stress plays an important role in the angular momentum transport. Second, the dependence of turbulent transport on the large-scale magnetic field is  $Re_M$ -dependent and can lead to enhanced quenching in the parameter regime studied here in comparison to earlier more laminar simulations. However, for a limited parameter range we find that the system vacillates between two states where either the differential rotation is strong and mean magnetic field relatively weak or vice versa. Furthermore, the temporal variations appear to increase as the Rayleigh and Reynolds numbers are increased. Finally, we find that in cases where the differential rotation is anti-solar, the quenching is much less prominent, possibly due to significantly weaker mean fields generated in those cases.

The total magnetic energy grows monotonically as a function of  $Re_M$  in all of our runs. The energy of the azimuthally averaged fields is in all cases consistent with *increasing or constant* mean fields at high  $Re_M$ . This is apparently at odds with the anelastic full-sphere simulations of Nelson et al. (2013) who found a steeply declining trend with magnetic Reynolds number. However, their relatively rapidly rotating ( $\Omega = 3\Omega_\odot$ ) simulations allow also significant low-order non-axisymmetric modes

than in the time average over the full duration (50 years) of the simulation.

to develop that will not show up in azimuthal averaging. A fair comparison is thus not possible without a proper assessment of the non-axisymmetric contributions. Our results are more in line with those of Hotta et al. (2016) who use a model rotating at the solar rate where the large-scale fields are more clearly axisymmetric.

A possible source of discrepancies between the current and previous studies is the use of wedge geometry. Rigorous comparisons between wedges and fully spherical simulations have not been done so far. However, runs with similar parameters (Rayleigh, Taylor, and Prandtl numbers) produce results that are in qualitative agreement; compare, e.g., the results of Käpylä et al. (2010b) regarding cyclic dynamos with those of Brown et al. (2011). Similarly, the more recent simulations showing equatorward migration (Käpylä et al. 2012; Augustson et al. 2015) appear to support the validity of the wedge approach. Furthermore, wedges with full  $2\pi$  extent in longitude produce dynamos dominated by non-axisymmetric large-scale fields with azimuthal dynamo waves (Käpylä et al. 2013; Cole et al. 2014) that are also routinely seen in anelastic full sphere simulations (e.g. Yadav et al. 2015). Lastly, the transition from anti-solar to solar-like differential rotation occurs at very similar Coriolis numbers in a wide range of simulations, including wedges with artificially increased luminosity and rotation rate (Gastine et al. 2014). The various modeling approaches also use a range of different subgrid-scale models and parameter values (see Tables A.1 and A.2 in Appendix A) and are still able to reproduce similar large-scale phenomena. These comparisons suggest that the current results obtained in wedges are likely to be realized in fully spherical simulations in the same parameter regime.

Our final conclusion is that the current simulations are not near an asymptotic regime where the large-scale results would be independent of the microphysical diffusion coefficients. This is most strikingly demonstrated by the steep quenching of the differential rotation and the disappearance of regularly oscillating large-scale magnetic fields at high values of  $Re_M$ .

*Acknowledgements.* The authors thank an anonymous referee for useful comments and Paul Charbonneau and Hideyuki Hotta for providing information regarding their models. The simulations were performed using the supercomputers hosted by CSC – IT Center for Science Ltd. in Espoo, Finland, who are administered by the Finnish Ministry of Education and in the HLRS supercomputing center in Stuttgart, Germany through the PRACE allocation ‘SOLDYN.’ Financial support from the Academy of Finland grants No. 136189, 140970, 272786 (PJK), and 272157 to the ReSoLVE Centre of Excellence (PJK, MJK), as well as the Swedish Research Council grants 621-2011-5076 and 2012-5797, and the Research Council of Norway under the FRINATEK grant 231444 are acknowledged. JW acknowledges funding by the Max-Planck/Princeton Center for Plasma Physics and funding from the People Programme (Marie Curie Actions) of the European Union’s Seventh Framework Programme (FP7/2007-2013) under REA grant agreement No. 623609.

## References

- Augustson, K., Brun, A. S., Miesch, M., & Toomre, J. 2015, ApJ, 809, 149
- Blackman, E. G. & Brandenburg, A. 2003, ApJ, 584, L99
- Brandenburg, A. 2001, ApJ, 550, 824
- Brandenburg, A., Candelaresi, S., & Chatterjee, P. 2009, MNRAS, 398, 1414
- Brandenburg, A., Chan, K. L., Nordlund, Å., & Stein, R. F. 2005, AN, 326, 681
- Brandenburg, A. & Dobler, W. 2001, A&A, 369, 329
- Brandenburg, A. & Sandin, C. 2004, A&A, 427, 13
- Brown, B. P., Browning, M. K., Brun, A. S., Miesch, M. S., & Toomre, J. 2010, ApJ, 711, 424
- Brown, B. P., Miesch, M. S., Browning, M. K., Brun, A. S., & Toomre, J. 2011, ApJ, 731, 69
- Brun, A. S., Miesch, M. S., & Toomre, J. 2004, ApJ, 614, 1073
- Busse, F. H. 2002, Phys. Fluids, 14, 1301

Busse, F. H. & Simitev, R. D. 2006, *Geophys. Astrophys. Fluid Dynam.*, 100, 341  
 Cattaneo, F. 1999, *ApJ*, 515, L39  
 Cattaneo, F. & Hughes, D. W. 1996, *Phys. Rev. E*, 54, 4532  
 Cattaneo, F. & Vainshtein, S. I. 1991, *ApJ*, 376, L21  
 Cole, E., Brandenburg, A., Käpylä, P. J., & Käpylä, M. J. 2016, *A&A*, in press, arXiv:1601.05246  
 Cole, E., Käpylä, P. J., Mantere, M. J., & Brandenburg, A. 2014, *ApJL*, 780, L22  
 Del Sordo, F., Guerrero, G., & Brandenburg, A. 2013, *MNRAS*, 429, 1686  
 Duarte, L. D. V., Wicht, J., Browning, M. K., & Gastine, T. 2016, *MNRAS*, 456, 1708  
 Gastine, T., Duarte, L., & Wicht, J. 2012, *A&A*, 546, A19  
 Gastine, T., Yadav, R. K., Morin, J., Reiners, A., & Wicht, J. 2014, *MNRAS*, 438, L76  
 Ghizaru, M., Charbonneau, P., & Smolarkiewicz, P. K. 2010, *ApJ*, 715, L133  
 Gilman, P. A. 1983, *ApJS*, 53, 243  
 Glatzmaier, G. A. 1985, *ApJ*, 291, 300  
 Gruzinov, A. V. & Diamond, P. H. 1995, *Physics of Plasmas*, 2, 1941  
 Hotta, H., Rempel, M., & Yokoyama, T. 2016, *Science*, 351, 1427  
 Hotta, H., Rempel, M., Yokoyama, T., Iida, Y., & Fan, Y. 2012, *A&A*, 539, A30  
 Jennings, R., Brandenburg, A., Tuominen, I., & Moss, D. 1990, *A&A*, 230, 463  
 Käpylä, M. J., Käpylä, P. J., Olsper, N., et al. 2016a, *A&A*, 589, A56  
 Käpylä, P. J. & Brandenburg, A. 2008, *A&A*, 488, 9  
 Käpylä, P. J., Brandenburg, A., Kleorin, N., Käpylä, M. J., & Rogachevskii, I. 2016b, *A&A*, 588, A150  
 Käpylä, P. J., Käpylä, M. J., & Brandenburg, A. 2014, *A&A*, 570, A43  
 Käpylä, P. J., Korpi, M. J., & Brandenburg, A. 2010a, *A&A*, 518, A22  
 Käpylä, P. J., Korpi, M. J., Brandenburg, A., Mitra, D., & Tavakol, R. 2010b, *Astron. Nachr.*, 331, 73  
 Käpylä, P. J., Mantere, M. J., & Brandenburg, A. 2011a, *Astron. Nachr.*, 332, 883  
 Käpylä, P. J., Mantere, M. J., & Brandenburg, A. 2012, *ApJ*, 755, L22  
 Käpylä, P. J., Mantere, M. J., Cole, E., Warnecke, J., & Brandenburg, A. 2013, *ApJ*, 778, 41  
 Käpylä, P. J., Mantere, M. J., Guerrero, G., Brandenburg, A., & Chatterjee, P. 2011b, *A&A*, 531, A162  
 Karak, B. B., Käpylä, P. J., Käpylä, M. J., et al. 2015, *A&A*, 576, A26  
 Lindborg, M., Mantere, M. J., Olsper, N., et al. 2013, *A&A*, 559, A97  
 Masada, Y. 2011, *MNRAS*, 411, L26  
 Mitra, D., Tavakol, R., Brandenburg, A., & Moss, D. 2009, *ApJ*, 697, 923  
 Nelson, N. J., Brown, B. P., Brun, A. S., Miesch, M. S., & Toomre, J. 2013, *ApJ*, 762, 73  
 Olsper, N., Käpylä, M. J., Pelt, J., et al. 2015, *A&A*, 577, A120  
 Parfrey, K. P. & Menou, K. 2007, *ApJ*, 667, L207  
 Parker, E. N. 1955, *ApJ*, 121, 491  
 Passos, D. & Charbonneau, P. 2014, *A&A*, 568, A113  
 Pelt, J. 1983, in *ESA Special Publication*, Vol. 201, *Statistical Methods in Astronomy*, ed. E. J. Rolfe, 37–42  
 Rüdiger, G. 1980, *Geophys. Astrophys. Fluid Dynam.*, 16, 239  
 Rüdiger, G. 1989, *Differential Rotation and Stellar Convection. Sun and Solar-type Stars* (Berlin: Akademie Verlag)  
 Schekochihin, A. A., Haugen, N. E. L., Brandenburg, A., et al. 2005, *ApJ*, 625, L115  
 Schrunner, M., Petitdemange, L., & Dormy, E. 2011, *A&A*, 530, A140  
 Schrunner, M., Petitdemange, L., & Dormy, E. 2012, *ApJ*, 752, 121  
 Shukurov, A., Sokoloff, D., Subramanian, K., & Brandenburg, A. 2006, *A&A*, 448, L33  
 Simitev, R. & Busse, F. H. 2005, *J. Fluid Mech.*, 532, 365  
 Smolarkiewicz, P. K. & Charbonneau, P. 2013, *J. Comp. Phys.*, 236, 608  
 Stix, M. 2002, *The Sun: An Introduction* (Springer, Berlin)  
 Strugarek, A., Beaudoin, P., Brun, A. S., et al. 2016, *ASR*, in press, arXiv:1605.08685  
 Sur, S., Shukurov, A., & Subramanian, K. 2007, *MNRAS*, 377, 874  
 Vainshtein, S. I. & Cattaneo, F. 1992, *ApJ*, 393, 165  
 Warnecke, J. & Brandenburg, A. 2014, in *IAU Symposium*, Vol. 302, *IAU Symposium*, ed. P. Petit, M. Jardine, & H. C. Spruit, 134–137  
 Warnecke, J., Brandenburg, A., & Mitra, D. 2011, *A&A*, 534, A11  
 Warnecke, J., Brandenburg, A., & Mitra, D. 2012, *J. Spa. Weather Spa. Clim.*, 2, A11  
 Warnecke, J., Käpylä, P. J., Käpylä, M. J., & Brandenburg, A. 2014, *ApJ*, 796, L12  
 Warnecke, J., Käpylä, P. J., Käpylä, M. J., & Brandenburg, A. 2016a, *A&A*, in press, arXiv:1503.05251  
 Warnecke, J., Rheinhardt, M., Käpylä, P. J., Käpylä, M. J., & Brandenburg, A. 2016b, *A&A*, submitted, arXiv:1601.03730  
 Yadav, R. K., Gastine, T., Christensen, U. R., & Reiners, A. 2015, *A&A*, 573, A68  
 Yoshimura, H. 1975, *ApJ*, 201, 740

## Appendix A: Comparison to other simulation methods

The purpose of this appendix is to compare the diffusion schemes and estimates of the Prandtl number in the present study with several methods presented in the literature. We consider the papers by Nelson et al. (2013) and Hotta et al. (2016) that are discussed in the main text as well as the study of Ghizaru et al. (2010) that represents another established simulation method; see Tables A.1 and A.2 for details.

Estimating the Prandtl number from simulations using the solar luminosity requires that the value of the radiative diffusivity in the solar convection zone is known. For the following we use an estimate of this quantity at  $r = 0.85R_{\odot}$ . Standard solar models (e.g. Stix 2002) indicate that radiation carries roughly ten per cent of the flux at this radius such that  $L^{\text{rad}} \approx 0.1L_{\odot}$ . Using Eq. (6) we can write

$$L^{\text{rad}} = 4\pi r^2 F^{\text{rad}} = -4\pi r^2 K \partial_r T. \quad (\text{A.1})$$

We then use the definition of the heat conductivity  $K = c_P \rho \chi$ , assume that the temperature gradient is close to the adiabatic one,  $\partial_r T \approx -g/c_P$ , and insert  $g = GM_{\odot}/r^2$  to obtain

$$\chi = \frac{L^{\text{rad}}}{4\pi GM_{\odot} \rho}. \quad (\text{A.2})$$

Using the values quoted above and  $\rho \approx 50 \text{ kg m}^{-3}$  (Stix 2002) we find that  $\chi \approx 5 \cdot 10^2 \text{ m}^2 \text{ s}^{-1}$  for the Sun at  $r = 0.85R_{\odot}$ .

The solar luminosity is adopted in the study of Nelson et al. (2013), yielding a radiative diffusion coefficient of the order of the estimate Eq. (A.2). They, however, do not present a detailed description of their model but refer to Brown et al. (2010) where the corresponding quantity is denoted as  $\kappa_r$ . Furthermore, the values of  $\nu$  at mid-convection zone depth are in the range  $6 \dots 13 \cdot 10^7 \text{ m}^2 \text{ s}^{-1}$  for their Cases D3[a,b,pm1,pm2] and a value of  $2 \cdot 10^6 \text{ m}^2 \text{ s}^{-1}$  is estimated for Case S3 with a Smagorinsky SGS model. These yield Prandtl numbers of the order of  $10^5$  and  $10^4$ , respectively. For the model ‘Low’ of Hotta et al. (2016), only the surface value  $\nu = 10^8 \text{ m}^2 \text{ s}^{-1}$  is given. As  $\nu$  is proportional to  $\rho^{-1/2}$ , the value at mid-convection zone depth is a few times  $10^7 \text{ m}^2 \text{ s}^{-1}$  and the Prandtl number is of the order of  $10^5$ . For their cases ‘Medium’, ‘High’, and ‘High-S’, a slope-limited diffusion scheme is used, so estimating the diffusion coefficients is non-trivial. However, they compute the Reynolds number (hereafter  $\text{Re}_{\text{SL}}$ ) based on the Taylor microscale that was obtained from kinetic energy spectra. They find that the Reynolds numbers for ‘High’ and ‘High-S’ are roughly an order of magnitude larger than for ‘Low’, whereas for ‘Low’ and ‘Medium’ they are comparable. Assuming that the turbulent velocities in all cases are of similar strengths, we can estimate ‘slope-limited diffusion viscosities’ from  $\nu_{\text{SL}} = \nu_{\text{Low}} \text{Re}_{\text{Low}}/\text{Re}_{\text{SL}}$ . We thus infer that the value of the Prandtl number in the model ‘Medium’ is  $10^5$  and an order of magnitude smaller in the models ‘High’ and ‘High-S’. In these runs, the surface value of the turbulent heat conductivity is  $\kappa = 2 \cdot 10^9 \text{ m}^2 \text{ s}^{-1}$  (H. Hotta, private communication), yielding  $\text{Pr}_{\text{SGS}}$  in the range  $0.05 \dots 2 \cdot 10^{-3}$  for the runs of Hotta et al. (2016).

In principle even a third Prandtl number can be defined based on the diffusion coefficient applied only to the mean (spherically symmetric) entropy profile. In the present study and also in that of Hotta et al. (2016), this coincides with the coefficient relevant for diffusing entropy fluctuations. However, the coefficients can also be different which is the formulation often used in simulations performed with the Anelastic Spherical Harmonic (ASH)

code including those presented in Nelson et al. (2013). However, the value of the coefficient for mean entropy diffusion ( $\kappa_0$ ) is not provided in the reference with a more detailed model description (Brown et al. 2010).

The Eulerian-Lagrangian (EULAG) code of Smolarkiewicz & Charbonneau (2013) employed by Ghizaru et al. (2010) uses quite a different approach and replaces radiative conduction by Newtonian cooling toward a prescribed thermodynamic state. The timescale of the cooling  $\tau_c$  is typically of the order of 20 years (P. Charbonneau, private communication; see also Strugarek et al. 2016). This timescale would correspond to a radiative/SGS diffusion coefficient of  $\chi = \Delta r^2 / \tau_c \approx 5 \cdot 10^7 \text{ m}^2 \text{ s}^{-1}$ , where  $\Delta r = 0.25 R_\odot$ . Although this comparison yields some insight about the entropy evolution, the cooling and diffusion processes cannot be directly equated. Therefore the concept of a Prandtl number does not appear suitable in that case. The diffusion of velocity, magnetic fields, and entropy fluctuations is due to the numerical scheme making the estimates of the other Prandtl numbers also problematic. Presumably the diffusivities of all variables at a given resolution are roughly similar such that  $\text{Pr}_{\text{SGS}}$  and  $\text{Pr}_{\text{M}}$  are of the order of unity. Hydrodynamic EULAG models with an otherwise similar setup to that of Ghizaru et al. (2010) yield estimates of viscosity and entropy diffusion in ranges  $\nu_{\text{eff}} = 0.6 \dots 1.2 \cdot 10^8 \text{ m}^2 \text{ s}^{-1}$  and  $\kappa_{\text{eff}} = 1 \dots 8 \cdot 10^7 \text{ m}^2 \text{ s}^{-1}$ , respectively, with  $\text{Pr}_{\text{SGS}} = \nu_{\text{eff}} / \kappa_{\text{eff}} \approx 1 \dots 8$  (Strugarek et al. 2016).

We show the conversion factors for the definitions used in the current study for Péclet, fluid and magnetic Reynolds, and Coriolis numbers in Table A.2. The conversion for the results of Nelson et al. (2013) is straightforward, except that for the Coriolis number we have used the relation  $\text{Ta} = \text{Co}'^2 \text{Re}'^2$  to compute  $\text{Co}' = 2\pi \text{Co}$ . The definition of the Rossby number in Nelson et al. (2013),  $\text{Ro} = \omega / 2\Omega$ , is based on the vorticity  $\omega = \nabla \times \mathbf{u}$  and corresponds to  $\text{Co} = \text{Ro}^{-1} k_\omega / k_f$ , where  $k_\omega = \omega_{\text{rms}} / u_{\text{rms}}$ . The values of  $\text{Co}$  for the models of Nelson et al. (2013) correspond well to our simulations with  $\Omega = 3\Omega_\odot$ , see Table 1. In the case of the EULAG simulations we use the values quoted by Passos & Charbonneau (2014) for the Reynolds numbers (30 ... 60 in their notation) divided by  $2\pi$  and the estimate of  $\text{Pr}_{\text{SGS}}$  quoted above to compute  $\text{Pe}$ . The estimate of the Coriolis number is based on simulation data provided by P. Charbonneau. Finally, for the study of Hotta et al. (2016), the conversion of the fluid and magnetic Reynolds numbers is based on values given in the paper whereas the estimates of  $\text{Pe}$  and  $\text{Co}$  are based on simulation data provided by H. Hotta. The values of  $\text{Co}$  are again in excellent agreement with our corresponding simulations with  $\Omega = \Omega_\odot$ ; see Table 1.

We note that the simulations of Nelson et al. (2013) and Hotta et al. (2016) operate in a low- $\text{Pr}_{\text{SGS}}$  regime which is also realized in the Sun, although in a much more extreme fashion. Such a regime is required especially in simulations with solar luminosity and rotation rate to lower the convective velocities and to achieve solar-like differential rotation (Käpylä et al. 2014; Hotta et al. 2016). However, the tradeoff is that the Péclet numbers are low and the evolution of entropy is significantly influenced by the SGS diffusion. It is not clear whether such an approach is more realistic in comparison to having  $\text{Pr}_{\text{SGS}}$  and  $\text{Pr}_{\text{M}}$  of the order of unity and  $\text{Re}$ ,  $\text{Re}_{\text{M}}$ , and  $\text{Pe} \gg 1$ . We also note that the run times of the highest resolution runs are short: 4 years for ‘S3’ in Nelson et al. (2013) and 500 days for ‘High-S’ in Hotta et al. (2016), whereas transients and/or secular evolution in the high- $\text{Re}_{\text{M}}$  regime can have a significantly longer timescale; see Fig. 3(b)-(d).

**Table A.1.** Diffusion schemes applied in a few comparable studies.

Study	Viscosity	Magnetic diffusivity	Radiative diffusion	Mean entropy diffusion	Fluctuating entropy diffusion
Present work (PENCIL CODE)	$\nu$ (constant)	$\eta$ (constant)	$\chi$ ( $6.4 \cdot 10^5 \times$ solar)	$\chi_{\text{SGS}}$ (piecewise constant)	$\chi_{\text{SGS}}$ (piecewise constant)
Nelson et al. (2013), (ASH) Cases D3[a,b,pm1,pm2]	$\nu$ ( $\propto \rho^{-1/2}$ )	$\eta$ ( $\propto \rho^{-1/2}$ )	$\kappa_r$ (solar)	$\kappa_0$ (near surface)	$\kappa$ ( $\propto \rho^{-1/2}$ )
Nelson et al. (2013), Case S3	$\nu_S$ Smagorinsky	$\eta_S \equiv \nu_S/\text{Pm}$ Smagorinsky	$\kappa_r$ (solar)	$\kappa_0$ (near surface)	$\kappa_S \equiv \nu_S/\text{Pr}$ Smagorinsky
Ghizaru et al. (2010) (EULAG)	iLES	iLES	Newtonian cooling	Newtonian cooling	iLES+Newtonian cooling
Hotta et al. (2016) Low	$\nu$ ( $\propto \rho^{-1/2}$ )	$\eta$ ( $\propto \rho^{-1/2}$ )	$\kappa_r$ (solar)	$\kappa$ ( $\propto \rho^{-1/2}$ )	$\kappa$ ( $\propto \rho^{-1/2}$ )
Hotta et al. (2016) Medium, High, High-S	Slope-limited diffusion	Slope-limited diffusivity	$\kappa_r$ (solar)	$\kappa$ ( $\propto \rho^{-1/2}$ )	$\kappa$ ( $\propto \rho^{-1/2}$ )

**Notes.** The entries for each study correspond to the symbols used for the various diffusion coefficients and their spatial profiles or functional dependences, where applicable. The coefficients  $\kappa_r$  and  $\kappa_0$  are not mentioned in the paper by Nelson et al. (2013) who refer to an earlier study by Brown et al. (2010) for a detailed description of their model. iLES stands for implicit Large-Eddy Simulation where the truncation errors of the numerical scheme provide the diffusion.

**Table A.2.** Parameter values with conversion factors to the definition in the present study from the same studies as in Table A.1.

Study	Pr	Pr <sub>SGS</sub>	Pr <sub>M</sub>	Pe	Re	Re <sub>M</sub>	Co
Present work	18...72	0.25...5	0.5...5	4...134	17...134	5...151	1.4...15.9
Nelson et al. (2013), (ASH) Cases D3[a,b,pm1,pm2]	$\nu/\kappa_r$ $\mathcal{O}(10^5)$	$\nu/\kappa$ 0.25	$\nu/\eta$ 0.5...2	$\text{PrRe}'/(2\pi)$ 4...11	$\text{Re}'/(2\pi)$ 16...43	$\text{Rm}'/(2\pi)$ 8...22	$\sqrt{\text{Ta}}/(2\pi\text{Re}')$ 4.5...5.5
Nelson et al. (2013), Case S3	$\nu_S/\kappa_r$ $\mathcal{O}(10^4)$	$\nu_S/\kappa_S$ 0.25	$\nu_S/\eta_S$ 0.5	$\text{PrRe}'/(2\pi)$ 229	$\text{Re}'/(2\pi)$ 915	$\text{Rm}'/(2\pi)$ 458	$\sqrt{\text{Ta}}/(2\pi\text{Re}')$ 5.8
Ghizaru et al. (2010) (EULAG)	?	$\approx 1$	$\approx 1$	5...10	5...10	5...10	30
Hotta et al. (2016) Low	$\nu/\kappa_r$ $\mathcal{O}(10^5)$	$\nu/\kappa$ 0.05	$\nu/\eta$ 1	$\text{PrRe}/(2\pi)$ 2.5	$\text{Re}/(2\pi)$ 51	$\text{PmRe}/(2\pi)$ 51	1.4
Hotta et al. (2016) Medium, High, High-S	$\nu_{\text{SL}}/\kappa_r$ $\mathcal{O}(10^4 \dots 10^5)$	$\nu_{\text{SL}}/\kappa$ $0.04 \dots 2 \cdot 10^{-3}$	$\nu_{\text{SL}}/\eta_{\text{SL}}$ 1.03...1.71	$\text{PrRe}/(2\pi)$ 2.5	$\text{Re}/(2\pi)$ 61...1129	$\text{PmRe}/(2\pi)$ 63...1930	1.4

**Notes.** Question marks indicate quantities not described in the respective papers. In the last row,  $\nu_{\text{SL}}$  and  $\eta_{\text{SL}}$  are the viscosity and magnetic diffusivity estimated from their slope-limited diffusion scheme (see text). The values for Pe, Re, and Re<sub>M</sub> for the study of Ghizaru et al. (2010) are based on values stated in Passos & Charbonneau (2014) divided by  $2\pi$ . The Coriolis numbers for the simulations of Ghizaru et al. (2010) and Hotta et al. (2016) were calculated using our definition, Eq. (22), and simulation data for the volume averaged rms-value of velocity fluctuations provided by P. Charbonneau and H. Hotta, respectively.